Computational Fluid Dynamics in Patient-Specific Models of Normal and Chiari I Geometries

by

Gabriela Rutkowska

MASTER THESIS
for the degree of

Master in Computational Science and Engineering

Faculty of Mathematics and Natural Sciences
UNIVERSITY OF OSLO

June 6th, 2011

Acknowledgements

First of all, I would like to express my gratitude to my two supervisors; Kent-Andre Mardal and Svein Linge. Thank you for your thorough guidance, valuable advice, support and encouragement. Your enthusiasm and optimism gave me a lot of motivation. Next, I would like to thank Victor Haughton for providing MRI-measurements, patient-data and articles as well as for his constructive and encouraging feedback on the thesis. Thanks to Karen-Helene Støverud for help with MRI-scans, medical literature and for other helpful advice. Also, thanks to Simula Research Laboratory for providing the computer resources necessary for all the heavy simulations.

The model generation in VMTK would not have been possible without Luca Antiga's valuable contribution - thank you for the immediate help with model capping and for other advice on VMTK.

A big thank you to my fellow students for the fantastic social environment and many great memories through the last five years. Especially Eline and Øyvind, thank you for all your help and for keeping my spirits up whenever I needed it. Last but not least, I would like to thank my mother and Ola for constant love and support. I would not have managed this without you!

Gabriela Rutkowska

June, 2011

Abstract

Chiari I malformation characterizes by cerebellar tonsils submerging below foramen magnum, leading to obstruction of subarachnoid space (SAS) that alters the cerebrospinal fluid (CSF) flow. The condition leads to diverse symptoms in patients and is in some cases accompanied by a syrinx in the spinal cord. In order to improve the understanding of effects of SAS geometry on the CSF flow characteristics, numerical simulations of the CSF flow were conducted on a a series of personalized models of Chiari I patients, healthy volunteers and post-operative patients. The models were generated with the help of VMTK, which is a software tool for reconstruction of anatomical structures based on segmentation of medical images. To simulate the CSF flow, we applied the Navier Stokes equations for incompressible Newtonian fluid, which were solved numerically by applying the Finite Element Method (FEM) to the Incremental Pressure Correction Scheme (IPCS). The simulations were conducted by means of a pre-provided code for computational fluid dynamics (CFD) based on the FEniCS software library. To assess the validity of our results, the computed velocities were compared with MRI-measurements of the studied patients. If the computations were significantly different from the velocity measurements, the inflow and outflow conditions were changed accordingly and new simulations were conducted. Chiari I models have shown more evident flow complexities, greater peak velocities, higher flux-values and larger magnitude of bidirectional flow compared to models of healthy volunteers. We observed that to achieve more realistic results in future simulations, setting pressure and velocity conditions based on MRI measurements is recommended.

List of contents

Chapter 1

Introduction

Technology and science have progressed at an accelerated rate during the last century, giving us a possibility to study and explore our surroundings from the smallest particles to the distant regions of the universe. Despite this, the phenomenon that seems to be the easiest accessible for us; our own body, has still not been fully understood. The human body is an astoundingly complex biologic machine with inter-related physiological functions. A thorough understanding of the biological mechanisms involved is crucial for accurate treatment of the different kinds of malfunctioning which can occur in this complicated system. Even with the advanced tools of today, many aspects of the human body are difficult to explore in a detailed but noninvasive way due to their inaccessibility and vulnerability. However, the development of computational science has made it possible to reconstruct and simulate phenomena which are difficult or impossible to observe in real life. The advancement of computational fluid dynamics (CFD) gives limitless applications in medicine, from modeling human physiology to analyzing a patient's air or blood flow without causing any threat to patient health. This study gives an example of this noninvasive approach, applying CFD to advance our understanding of issues related to the Chiari I malformation.

Chiari I malformation is a serious neurological condition that affects the delicate regions of the brain and the spinal cord (see Chapter 2 on Medical Background). Its description originates from a study by Hans Chiari in 1891, and the condition has since been studied by many (see e.g. Bejjani (2001) and references therein). Chiari I malformation is characterized by cerebellar tonsils submerging below the foramen magnum. The herniated tonsils alter the flow of cerebrospinal fluid (CSF) that surrounds the brain and the spinal cord and pulsates up and down through foramen magnum with every heartbeat. The malformation may cause a whole range of symptoms, from headache to more serious neurological disorders (Mueller and Oró, 2004). Often, it is accompanied by a cyst (syrinx) in the spinal cord, a condition called syringomyelia (Heiss et al., 1999) It is believed that the syrinx-formation is a direct consequence of the malformation, somehow triggered by the altered CSF flow.

Previously regarded as a rare condition, the reports of Chiari I malformation have increased sharply due to the advanced availability of magnetic resonance imaging (MRI). It is currently estimated that about 0.1-0.6% of the American population suffers from the Chiari I malformation (*http://www.chiariinstitute.com*). If left untreated, the progressing Chiari malformation may have a lethal outcome (Stephany et al., 2008). When necessary, the condition is treated by surgery. However, there is no guarantee that the surgery makes Chiari symptoms disappear. The diagnosis and treatment of Chiari has yet to be standardized . Even 16 years after their publication this quotation by Ball and Crone (1995) still seems to be relevant: *"Ever since the initial postmortem description by Chiari in 1891 of the group of malformations that bears his name, it seems there have always been more questions on this subject than answers.*"

The triggers and the mechanisms behind Chiari I malformation and syringomyelia development are still subject to controversy. The inaccessibility of the brain and spinal cord regions has made it hard to reach conclusions. Moreover, the CSF flow cannot be assessed in post-mortem studies, as the vital mechanisms have terminated. In 1999, Chiari Institute surgeons were the first to adapt color Doppler ultrasonography for the intraoperative measurement of CSF flow (e.g. Milhorat and Bolognese (2003)). Yet, a less obtrusive investigation technique that does not involve surgery is necessary. The development of Phase-contrast MR (PC MRI) (e.g. Battal et al. (2011), Quigley et al. (2004)) has benefited the knowledge of CSF dynamics, but suffer bad resolution in space and time. The recent introduction of CFD provides a means to analyze CSF flow patterns for a whole volume of interest with good temporal resolution. Linge et al. (2011) applied the CFD to idealized models, an approach that benefits from increased modeling freedom. Roldan et al. (2009) assessed the CSF flow on two patient-specific models, yielding detailed characterization of flow in a particular individual. Although his sample size was small, and applied an unphysiological unidirectional flow with constant velocity, it was one of the first studies to take on the challenge of patient-specific modeling.

The purpose of the present study is to advance our understanding of Chiari related issues by using CFD to study the cervical pulsatile flow of CSF in a whole series of personalized models of healthy volunteers, Chiari I patients, and post-operative patients.

This thesis has the following outline. Chapter 2 yields a brief introduction to the medical background concerning Chiari I malformation and syringomyelia. Chapter 3 gives a description of the mathematical model and the software tools. Results are presented in Chapter 5 before our findings are discussed in Chapter 6.

Chapter 2

Medical Background

.

2.1 Chiari I Malformation

2.1.1 Anatomy

The CSF is a water-like fluid produced in the choroid plexus of the brain, around blood vessels and along ventricular walls. It circulates in the subarachnoid space (SAS) surrounding the brain and the spinal cord and it also fills the ventricular system within the brain. The CSF plays an important role in moderating the pressure changes in the cranial vault caused by the expansion of blood vessels and brain during systole and the following contraction during diastole. Since the skull is rigid, this pulsatility drives the CSF flow so that during one cardiac cycle CSF is pumped down the spinal canal and then back into the cranial vault. As a result, pressure gradients and velocities of the CSF change during the cardiac cycle.

The SAS can be divided into a cranial and a spinal part which are connected at the level of the foramen magnum. The foramen magnum is a large opening in the occipital bone of the cranium. The shape of the SAS is complex at this level. Its outer boundary, defined by the cranial vault and cervical spinal canal, tapers. The brain stem, which connects the brain to the spinal cord, and the inferior portion of the brain (the cerebellum) form the inner boundary of the SAS. Since the anatomy of the inferior cerebellum occupies variable amounts of the SAS behind the brain stem, this portion of the SAS shows much individual variation. The cerebellar tissue at the bottom of the cerebellum is referred to as the cerebellar tonsils.

Extending downward from the brain, is the spinal cord. It is of cylindrical shape and has a blood circulation with arteries and veins passing through it. The spaces where these blood vessels penetrate the spinal cord are called perivascular spaces. The spinal cord lies within the vertebral column composed of thirty-three bones called vertebrae. These vertebrae are grouped into five regions: cervical, thoracic, lumbar, sacral and coccygeal.

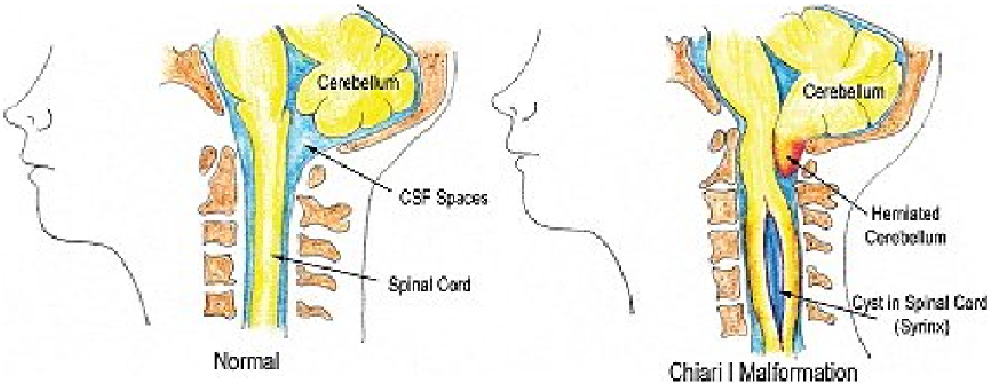

Figure 2.1: *The CSF spaces in a healthy individual (left) and in a patient with Chiari Malformation (right). Figure is taken from the web-page http://www.chiariinstitute.com*

2.1.2 The Malformation

Compared to healthy individuals, Chiari I patients have displacement of the cerebellar tonsils into the upper cervical spinal canal (Figure 2.1). This results in more complex CSF flow patterns than in healthy subjects. While in a healthy person, CSF flow has some inhomogeneity with small flow jets, CSF flow in Chiari patients has irregular and larger jets (Quigley et al., 2004). Maximum systolic and diastolic velocities occur in different locations in patients, while in healthy volunteers the maximum systolic and diastolic velocities occur in approximately the same regions. During time of maximal flow, higher velocities and pressure gradients are found in Chiari I patients than in normal subjects (e.g. Shah et al. (2011), Linge et al. (2011)).

2.1.3 Neurological manifestations of Chiari I

The Chiari I malformation affects the brain and the nervous system in a number of ways. Also, it modifies the CSF flow in the brain and elevates CSF pressure in the skull (Labuda, 2008). Consequently, the list of symptoms is very long. Different patients experience different symptoms, some more severe than others. The most common symptom is headache, which is often triggered by exertion, such as coughing, sneezing, laughing or standing up. Other common symptoms are dizziness, sleeping difficulties, weakness or numbness in arms, hands or legs, fatigue, neck pain, problems with vision, trouble with swallowing or respiration, tinnitus as well as weakened motor skills and balance problems (Mueller and Oró, 2004).

2.1.4 Diagnosis and treatment

MRI-scanning of the head effectively and non-invasively shows the position of the cerebellar tonsils. Tonsils extending more than 3-5 mm below the foramen magnum is the criterion used for diagnosis of the malformation. However, this criterion does not differentiate the symptomatic Chiari I malformation from the asymptomatic one, which applies to nearly half of the Chiari I cases. There are patients with severe symptoms who have tonsillar herniation of less than 3 mm and there are cases of asymptomatic patients with herniations larger than 3-5 mm (Labuda, 2008). Thus, the goal of the medical evaluation of Chiari I patients is to determine if their symptoms result from the Chiari I malformation and if they require surgery. The evaluation process includes MRI imaging of the spine to identify syringomyelia, Phase Contrast MRI to identify hyper-dynamic CSF flow, a careful history and neurological exam as well as clinical judgment and experience.

The surgery, called cranio-vertebral decompression, creates more room for the CSF flow. In the case of patients with Chiari I malformation only, approximately 80% of the surgeries lead to total cure of the symptoms or significant improvement (Hayhurst et al., 2008). For patients with syringomyelia, follow-up shows overall reduction of the syrinx in most cases (Lorenzo et al., 1995). Additionally, $95-97\%$ of patients have their symptoms improved or stabilized (Lorenzo et al., 1995; Xie et al., 2000), but $3-5\%$ deteriorated. The cranio-vertebral decompression may rarely have significant morbidity and may sometimes cause damage resulting in severe neurological defects. It is therefore crucial to improve our ability to identify the cause of signs and symptoms in patients with Chiari I.

2.2 Syringomyelia

Syringomyelia is characterized by formation and enlargement of tubular, fluid-filled cavities, called syrinxes, in the spinal cord. Syrinxes appear in connection with a number of conditions like spinal cord trauma and tumors. However, they appear most commonly as a result of the Chiari I malformation. Different estimates suggest that between 20% and 70% of cases with

Chiari I have syringomyelia (Labuda, 2008). Currently, there are no clear guidelines on how to predict which patients will develop a syrinx. Usual symptoms associated with this condition include pain, weakness or loss of sensations in arms and legs and inability to control the body temperature, often resulting in abnormal sweating and bladder and bowel problems. However, in some cases the syringomyelia does not produce any symptoms and is first discovered as a result of an MRI-scan. Syrinx-expansion may lead to damage in the nerve tissue in the spinal cord which again can cause permanent nerve damage and, in the worst case, paralysis.

There is a discussion among scientist about the source of the fluid in the syrinx. Most often, theories suggest that a syrinx consists of the CSF (Oldfield et al., 1994). However, some theories state that the syrinx consists of the extracellular fluid (Levine, 2004; Greitz, 2006). Also the mechanism behind the syrinx formation is a highly debated topic. Generally, physicians and medical scientists believe that the syrinx is related to the disturbance in CSF flow. However, a single widely accepted theory has yet to be articulated.

2.3 Theories for syringomyelia development

2.3.1 The Piston Theory

One of the theories of syringomyelia is the Piston Theory developed by Oldfield and Heiss (Oldfield et al., 1994; Heiss et al., 1999). It states that the cerebellar tonsils move during the cardiac cycle and act like a piston on the CSF. With each heart beat, the downward movement of the tonsils increase the pressure of the CSF. This drives the CSF into the spinal cord through the perivascular spaces.

The statements about tonsils being in movement are based on observations made during surgery. However, it is suspected that the tonsils move more during surgery than in normal conditions. PC MR research in this area shows that there is very little difference in tonsil movement of Chiari patients and control subjects (Levy, 2000; Cousins and Haughton, 2009). Overall, the tonsils move less than a millimeter in both groups. It might be questionable if such a small movement can have significant effect on the CSF flow. However, if flow boundaries are rigid enough, the incompressibility of the CSF will cause noticable effects on the flow even with minute tonsil motion. Heiss et al. (1999) estimates that the piston action of the tonsils is increased up to ten times in Chiari I patients.

Another criticism of the Piston theory (Levine, 2004) is that it does not explain how fluid entering the spinal cord causes the syrinx expansion. The theory assumes that mean pressure in the SAS is higher than the mean pressure in the syrinx. This assumption is not in agreement with measurements by e.g. Hall et al. (1980). However, it is possible that during the cardiac cycle, there are some brief periods when this necessary pressure relation occurs (Labuda, 2008).

2.3.2 Levine's theory

Another theory claims that activities such as coughing, straining or change in posture lead to higher CSF pressure in the skull than in the spine (Levine, 2004). The transmural venous and capillary pressure (which equals the blood pressure minus the pressure inside the tissue) changes corresponding to this imbalance. Above the subarachnoid obstruction, the transmural pressure is decreased, which results in collapse of blood vessels at this level. Below the obstruction, in the cord, the transmural pressure is increased, which leads to dilation of blood vessels. These spatially uneven changes in vessel caliber cause mechanical stress and damage to the spine. This results in partial disruption of the blood-spinal cord barrier which consists of tight junctions between capillary endothelial cells. Hypothetically, the junctions loosen because of the stress allowing fluid to leak from blood vessels into the spinal cord, creating a syrinx. Levine's theory has been criticized, for instance since the transmural venous and capillary pressure have never been measured.

2.3.3 Intramedullary Pulse Pressure Theory

The Intramedullary Pulse Pressure Theory is based on the Bernoulli theorem which states that a regional increase in fluid velocity in a narrowed flow channel decreases the pressure in the fluid (Greitz, 2006). The reduction in fluid pressure that results when a fluid flows through a constricted section of a channel is called the Venturi effect.

In Chiari I malformation with the tonsils positioned in the upper cervical spinal canal, CSF pressure gradients and velocities are increased. According to the Bernoulli theorem, this leads to decreased pressure in the narrow areas of the CSF-pathway. This creates a suction effect that, accordingly to the Greitz theory distends the cord during each systole. The distended cord fills with extracellular fluid, filling from the inside of the cord and creating a syrinx. Once formed, the syrinx decreases the cross-sectional area of the subarachnoid space, which in turn increases the Venturi effect, resulting in progression of the syrinx.

*

The three theories mentioned above yield further motivation for this study as they commonly propose that the pressure and velocities of the CSF are altered by the the SAS - geometry. Further, we intend to characterize tapering, pressure, velocities, synchronous bidirectional flow and flux in a series of personalized models. We generate 13 patient-specific geometries of identical anatomical regions of the SAS, starting at the occipital bone at foramen magnum down to the level above C6. The models represent three healthy individuals, six Chiari I patients and three post-operative patients. Additionally, one model of a non-symptomatic patient with tonsil-extensions measuring 2 mm is produced. As the tonsil extensions in the corresponding mesh turn out to be larger than 5 mm, we choose to classify this model into the Chiari-group. Patients include both males and females in the age-range of $2 - 54$ years.

Chapter 3

Methods

3.1 The Mathematical Model

3.1.1 CSF flow conditions

The simulations carried out in this thesis imitate the CSF flow through a region $\Omega \subset \mathbb{R}^3$ throughout time $t \in [0, t_{end}]$. The CSF flow can be modelled with viscosity and density similar to water under body-temperature (Hentschel et al., 2010a). The region surrounding the fluid is modelled as rigid and impermeable. The following table presents the values and parameters applied in the simulations in this study.

Table 3.1: Model variables and parameters

Symbol	Meaning	Unit	Chosen Value
u	velocity	$\frac{cm}{s}$	to be computed
p	pressure	Pa	to be computed
ρ	density	$\frac{kg}{cm^3}$	10^{-3}
ν	kinematic viscosity	$\frac{cm^2}{s}$	$0.700 \cdot 10^{-2}$[a]

[a] (Linge et al., 2011), water at 37^oC.

Initial condition
For simplicity, the flow in our simulations is started from rest. Hence, we impose the initial condition:

$$u = 0 \quad \forall \vec{x} = (x, y, z) \in \Omega, \quad t = 0$$

Starting CSF-flow simulations from an unphysical rest results in a transient phase since the flow needs some time to stabilize. Thus, the simulations are carried out for several cardiac cycles in order to reach a repeated flow pattern between the cycles. This is described further in the method-tests in Section 3.8.

Inflow and outflow conditions

The inflow and outflow conditions are specified by the pressure function which we set up on the basis of chosen peak pressure and peak pressure gradient. We choose the maximum pressure during systole to be $1961 Pa \approx 20\ cmH_2O$ (Linge et al., 2011). For the first round of simulations, the maximum difference in pressure between the top and the bottom of the model is selected to be

$$24.3\ Pa \approx 0.25\ cmH_2O, \ \text{(water at 4}^o\text{C)}.$$

for all models. Later, we will compare our computed velocities to MRI-measurements of the same patients and new simulations with modified pressure gradients will be conducted if our results are not verified by those measurements.

The coordinate system is chosen so that the systolic (caudad) flow is in negative z-direction, while the diastolic (cephalad) flow is in positive z-direction. Assuming a heart rate of 60 heart-beats per minute, the duration of one cardiac cycle is set to $1s$. The pressure distribution changes in z-direction and is asummed constant in the x- and y-directions. The pressure-function follows:

$$g(z,t) = (a - \frac{z_{max} - z}{z_{max} - z_{min}} b) \cdot sin(2\pi t) \tag{3.1}$$

where t is the time, $a = 1961\ Pa$, $b = 24.3\ Pa$ and z_{max} and z_{min} denote the z-coordinates of the top and the bottom of the model. The sinus-term is added to reproduce the pulsating motion of the fluid.

According to this pressure function, the flow changes direction during one cardiac cycle, so that the inflow and the outflow boundaries have the following definitions:

$$\partial\Omega_I = \begin{cases} \partial\Omega \cap \{z = z_{max}\}, & \text{t} \in [0, 0.5) \\ \partial\Omega \cap \{z = z_{min}\}, & \text{t} \in [0.5, 1.0) \end{cases}$$

$$\partial\Omega_O = \begin{cases} \partial\Omega \cap \{z = z_{min}\}, & \text{t} \in [0, 0.5) \\ \partial\Omega \cap \{z = z_{max}\}, & \text{t} \in [0.5, 1.0) \end{cases}$$

The inflow and outflow condition is thus the Dirichlet boundary condition

$$p = g(z,t) \quad \forall \vec{x} = (x,y,z) \in \partial\Omega_{IO}, \quad t \in (0, t_{end}]$$

where

$$\partial\Omega_{IO} = \partial\Omega_I \cup \partial\Omega_O$$

No-slip condition
The no-slip condition is given by

$$u = 0 \quad \forall \vec{x} = (x,y,z) \in \partial\Omega_D, \quad t \in [0, t_{end}]$$

where

$$\partial\Omega_D = \partial\Omega \setminus \partial\Omega_{IO}$$

3.1.2 The Navier Stokes Equations

To simulate CSF flow, we apply the Navier-Stokes equations for an incompressible Newtonian fluid,

$$\frac{\partial \vec{u}}{\partial t} + \nabla\vec{u} \cdot \vec{u} - \frac{1}{\rho}(\nabla \cdot \sigma) = \vec{f} \tag{3.2}$$

$$\nabla \cdot \vec{u} = 0 \tag{3.3}$$

where $\vec{u}$ is the unknown velocity, $\vec{f}$ denotes gravity and other body forces and the stress tensor σ equals

$$\sigma = -pI + 2\mu\epsilon \tag{3.4}$$

where p and ρ are given in Table 3.1, μ is the dynamic viscosity and ϵ is the symmetric strain tensor

$$\epsilon = \frac{1}{2}(\nabla\vec{u} + \nabla\vec{u}^T) \tag{3.5}$$

The Navier Stokes equations are derived from the conservation laws of mass and momentum. This derivation can be found in e.g. Griebel et al. (1998) but we present it below for completeness.

Conservation of mass
If $\rho(\vec{x}, t)$ is the density of a fluid at time t, then the mass of the fluid is given by the integral

$$\int_{\Omega_t} \rho(\vec{x},t)\ d\vec{x} \tag{3.6}$$

Starting at time $t = 0$, we have some amount of fluid occupying the domain Ω_0. As time goes by, the same amount of fluid will occupy the domain Ω_t. Hence, we have

$$\int_{\Omega_0} \rho(\vec{x},0)\ d\vec{x} = \int_{\Omega_t} \rho(\vec{x},t)\ d\vec{x} \quad \forall t \geq 0$$

Since the mass is constant in time, its derivative with respect to time must vanish.

$$\frac{d}{dt}\int_{\Omega_t} \rho(\vec{x},t)\ d\vec{x} = 0 \tag{3.7}$$

The transport theorem states that for a differentiable scalar function $f : \Omega_t \times [0, t_{end}] \to \mathbb{R}, (\vec{x},t) \to\ f(\vec{x},t)$ we have

$$\frac{d}{dt}\int_{\Omega_t} f(\vec{x},t)\ d\vec{x} = \int_{\Omega_t} \{\frac{\partial}{\partial t} f + \nabla \cdot (f\vec{u})\}(\vec{x},t)\ d\vec{x}$$

Applying the transport theorem to (3.7) results in

$$0 = \int_{\Omega_t} \{\frac{\partial \rho}{\partial t} + \nabla \cdot (\rho\vec{u})\}(\vec{x},t)\ d\vec{x} \quad \forall \vec{x} \in \Omega_t, \quad t \geq 0$$

Since this is valid for arbitrary regions Ω_t, the integrand vanishes. This yields

$$\frac{\partial}{\partial t}\rho + \nabla \cdot (\rho\vec{u}) = 0$$

However, since the CSF-fluid is incompressible (its density is constant), this reduces to

$$\nabla \cdot \vec{u} = 0$$

which is the continuity equation (3.3) for incompressible fluids.

Conservation of momentum

The momentum of a solid body is given by the product of its mass and its velocity. Using (3.6) to express the mass of the fluid, we express its momentum in the domain Ω_t by

$$\vec{m}(t) = \int_{\Omega_t} \rho(\vec{x}, t)\vec{u}(\vec{x}, t)\, d\vec{x} \tag{3.8}$$

According to Newton's second law, the time derivative of momentum equals the total force applied on the body:

$$\frac{D}{Dt}\vec{m}(t) = \sum_{i=1}^{N} \vec{F}_i$$

where $\frac{D}{Dt}$ is the material derivative:

$$\frac{D}{Dt}(\varphi) = \frac{\partial}{\partial t}(\varphi) + (\vec{u} \cdot \nabla)(\varphi)$$

The forces acting on the fluid are body forces and surface forces. The body forces, e.g. gravity, can be expressed as:

$$\int_{\Omega_t} \rho(\vec{x}, t)\vec{f}(\vec{x}, t)\, d\vec{x} \tag{3.9}$$

where $\vec{f}$ is a given force-density per unit volume. The surface forces, e.g. pressure and internal friction, can be represented by the equation

$$\int_{\partial\Omega_t} \sigma(\vec{x}, t)\vec{n}\, dS$$

where σ is a stress tensor which can be expressed as

$$\sigma = -pI + 2\mu\epsilon$$

Here p is the pressure, μ is the dynamic viscosity, ϵ is the strain tensor given by (3.5) and $\vec{n}$ is the outward pointing unit normal vector.

Using the divergence theorem, the expression for the surface forces can be reformulated accordingly:

$$\int_{\partial\Omega_t} \sigma(\vec{x}, t)\vec{n}\, dS = \int_{\Omega_t} \nabla \cdot \sigma(\vec{x}, t)\, d\vec{x} \tag{3.10}$$

Then, applying formulas (3.8), (3.9) and (3.10), Newton's second law can be rewritten to

$$\frac{D}{Dt}\int_{\Omega_t} \rho\vec{u}\;d\vec{x} = \int_{\Omega_t} (\rho\vec{f} + \nabla\cdot\sigma)\;d\vec{x}$$

Using the formula for the material derivative results in

$$\int_{\Omega_t} \frac{\partial}{\partial t}\rho\vec{u} + (\vec{u}\cdot\nabla)(\rho\vec{u})\;d\vec{x} = \int_{\Omega_t} (\rho\vec{f} + \nabla\cdot\sigma)\;d\vec{x}$$

This applies for arbitrary Ω_t so we can remove the integrals. Dividing with the density ρ yields

$$\frac{\partial}{\partial t}\vec{u} + (\vec{u}\cdot\nabla)\vec{u} - \frac{1}{\rho}(\nabla\cdot\sigma) = \vec{f}$$

which is the momentum equation (3.2) for incompressible fluids.

3.1.3 The Incremental Pressure Correction scheme (IPCS)

A numerical approach for solving Navier Stokes equations can often lead to unstable solutions. Valen-Sendstad et al. (2010) conducted a study on efficiency and accuracy of six different schemes for solving these equations. Their results suggest that IPCS is the most efficient and accurate of the tested schemes. Therefore, we choose to use this scheme in further implementation.

One of the challenges with the Navier Stokes equations is the coupling between velocity and pressure. The essence in the IPCS scheme is that the previous value for pressure is used to compute a tentative velocity which is later corrected. Hence, one unknown is removed from the equations.

Starting with the Navier Stokes equations (3.2) and (3.3) and letting Δt denote the time-step, we apply the backward Euler discretization scheme on the time derivative of u:

$$\frac{\partial u}{\partial t} \approx \frac{u^n - u^{n-1}}{\Delta t}$$

Further, the term for the stress tensor σ is discretized implicitly

$$\nabla\cdot\sigma \approx \nabla\cdot\sigma^n = 2\mu\nabla\cdot\epsilon(u^n) - \nabla p^n$$

while the convection-term $\nabla\vec{u}\cdot\vec{u}$, is discretized semi-implicitly in order to improve stability

$$\nabla u \cdot u \approx \nabla u^n \cdot u^{n-1}$$

The resulting discretization of (3.2) and (3.3) yields:

$$u^n + \Delta t \nabla u^n \cdot u^{n-1} + \frac{\Delta t}{\rho} \nabla p^n - 2\nu \Delta t \nabla \cdot \epsilon(u^n) - \Delta t f^n = u^{n-1} \tag{3.11}$$

$$\nabla \cdot u^n = 0 \tag{3.12}$$

where $\nu = \frac{\mu}{\rho}$. Further, we approximate u^n with the tentative velocity u^* where pressure from the previous step is used in the computation. In this manner, (3.11) turns into an elliptic equation:

$$u^* + \Delta t \nabla u^* \cdot u^{n-1} + \frac{\Delta t}{\rho} \nabla p^{n-1} - 2\nu \Delta t \nabla \cdot \epsilon(u^*) - \Delta t f^n = u^{n-1} \tag{3.13}$$

Subtracting (3.13) from (3.11) and letting u^c denote the velocity correction $u^c = u^n - u^*$ results in

$$u^c + \Delta t \nabla u^c \cdot u^{n-1} = - \frac{\Delta t}{\rho} \nabla (p^n - p^{n-1}) + 2\nu \Delta t \nabla \cdot \epsilon(u^c)$$

Since the error of this scheme is of order $O(\Delta t)$, we can simplify the above equation to

$$u^c = - \frac{\Delta t}{\rho} \nabla (p^n - p^{n-1}) \tag{3.14}$$

without further increasing the error. From (3.12) we know that

$$\nabla \cdot u^c = -\nabla \cdot u^* \tag{3.15}$$

which together with (3.14) yields a Poisson equation for the pressure difference $\Phi^n = p^n - p^{n-1}$,

$$\nabla^2 \Phi^n = \frac{\rho}{\Delta t} \nabla \cdot u^* \tag{3.16}$$

Solving this equation yields an expression for the corrected pressure

$$p^n = \Phi^n + p^{n-1} \tag{3.17}$$

and for the corrected velocity u^n

$$u^n = u^* - \frac{\Delta t}{\rho}\nabla(p^n - p^{n-1}) \tag{3.18}$$

where the tentative velocity u^* is computed by solving

$$\frac{u^* - u^{n-1}}{\Delta t} + \nabla u^* \cdot u^{n-1} = -\frac{1}{\rho}\nabla p^{n-1} + 2\nu\nabla \cdot \epsilon(u^*) + f^n \tag{3.19}$$

3.1.4 The Finite Element method

The Finite Element Method (FEM) (e.g. Logg et al. (2010)) is a flexible, numerical approach for solving partial differential equations. It easily handles geometrically complicated domains and makes it simple to construct higher-order approximations.

Starting with the IPCS scheme for the Navier-Stokes equations given in (3.16)-(3.19), the unknown velocity u^* and the pressure p^n are denoted as the trial functions in the trial spaces V and Q given by:

$$\begin{aligned} V &= \{v \in [H^1(\Omega)]^3 \ \mid \ v = 0 \ on \ \partial\Omega_D\} \\ Q &= \{v \in [H^1(\Omega)]^3 \ \mid \ v = g \ on \ \partial\Omega_{IO}\} \end{aligned}$$

where V is a vector function space, Q is a scalar function space, g is the pressure-function given in (3.1) and the Sobolev space $H^1(\Omega)$ is defined as:

$$H^1(\Omega) = \{f : \Omega \to \mathbb{R}^d \ \mid \ \int_\Omega f^2 + |\nabla f|^2 < \infty\}$$

We define two test-functions $v \in \hat{V}$ and $q \in \hat{Q}$ where the test spaces $\hat{V}$ and $\hat{Q}$ are given by

$$\begin{aligned} \hat{V} &= V \\ \hat{Q} &= \{v \in [H^1(\Omega)]^3 \ \mid \ v = 0 \ on \ \partial\Omega_{IO}\} \end{aligned}$$

where $\hat{V}$ is a vector function space and $\hat{Q}$ is a scalar function space. Multiplying (3.18) and (3.19) by v and (3.16) by q and integrating over the domain Ω yields

$$\int_\Omega u^n \cdot v \, d\Omega = \int_\Omega (u^* - \frac{\Delta t}{\rho}\nabla(p^n - p^{n-1})) \cdot v \, d\Omega$$

$$\int_\Omega \nabla^2 \Phi^n q \; d\Omega = \int_\Omega \frac{\rho}{\Delta t} \nabla \cdot u^* q \; d\Omega \tag{3.20}$$

$$\int_\Omega (\frac{u^* - u^{n-1}}{\Delta t} + \nabla u^* \cdot u^{n-1}) \cdot v \; d\Omega = \int_\Omega (\frac{1}{\rho} \nabla \cdot \sigma^n + f^n) \cdot v \; d\Omega \tag{3.21}$$

Applying integration by parts to (3.20) yields the pressure correction,

$$\int_\Omega \nabla p^n \nabla q \; d\Omega = \int_\Omega \nabla p^{n-1} \nabla q \; d\Omega - \int_\Omega \frac{\rho}{\Delta t} \nabla \cdot u^* q \; d\Omega$$

which holds for all q in the function space $\hat{Q}$.

Applying integration by parts to the first term on the right hand side of (3.21) yields

$$\begin{aligned}
\int_\Omega (\frac{1}{\rho} \nabla \cdot \sigma^n) \cdot v \; d\Omega =& \int_\Omega (\frac{1}{\rho} \nabla \cdot (-p^{n-1} + 2\mu\epsilon(u^*))v \; d\Omega \\
=& - \nu \int_\Omega (\nabla u^* + \nabla(u^{*T}))\nabla v \; d\Omega + \nu \int_{\partial\Omega} (\nabla u^* + \nabla(u^{*T}) \cdot nv \; dS \\
&+ \frac{1}{\rho} \int_\Omega p^{n-1} \nabla v \; d\Omega - \frac{1}{\rho} \int_{\partial\Omega} p^n v \cdot n \; dS \\
=& - \frac{1}{\rho} \int_\Omega \sigma^n \cdot \nabla v \; d\Omega - \frac{1}{\rho} \int_{\partial\Omega} p^{n-1} \cdot nv \; dS \\
&+ \int_{\partial\Omega} \nu(\nabla u^* + \nabla u^{*T}) \cdot nv \; dS
\end{aligned}$$

This holds for all v in the function space $\hat{V}$.

Using the inner product $\langle f, g \rangle = \int_\Omega fg \; d\Omega$, and the above calculations, the weak formulation of the Navier Stokes equations can thus be expressed as: Find $u \in V$ such that

$$\begin{aligned}
a_1(u^*, u^{n-1}, p^{n-1}, v) =& L_1(f^n, v), && \forall v \in \hat{V} && (3.22) \\
a_2(p^n, q) =& L_2(p^{n-1}, u^*, q), && \forall q \in \hat{Q} && (3.23) \\
a_3(u^n, v) =& L_3(u^*, p^{n-1}, p^n), && \forall q \in \hat{V} && (3.24)
\end{aligned}$$

where

$$\begin{aligned}
a_1(u^*, u^{n-1}, p^{n-1}, v) =& \langle v, \frac{u^* - u^{n-1}}{\Delta t} \rangle + \langle v, \nabla u^* \cdot u^{n-1} \rangle \\
&+ \langle \nabla v, \frac{1}{\rho} \sigma^n \rangle + \langle v, \frac{1}{\rho} p^{n-1} n \rangle_{\partial\Omega} \\
&- \langle v, \nu(\nabla u^* - \nabla u^{*T}) n \rangle_{\partial\Omega} && \forall v \in \hat{V} \\
L_1(f^n, v) =& \langle v, f^n \rangle && \forall v \in \hat{V} \\
a_2(p^n, q) =& \langle \nabla q, \nabla p^n \rangle && \forall q \in \hat{Q} \\
L_2(p^{n-1}, u^*, q) =& \langle \nabla q, \nabla p^{n-1} \rangle - \frac{\rho}{\Delta t} \langle q, \nabla \cdot u^* \rangle \ \&\forall q \in \hat{Q} \\
a_3(u^n, v) =& \langle v, u^n \rangle && \forall v \in \hat{V} \\
L_3(u^*, p^n, p^{n-1}, v) =& \langle v, u^* \rangle - \frac{\Delta t}{\rho} \langle v, \nabla(p^n - p^{n-1}) \rangle && \forall v \in \hat{V}
\end{aligned}$$

In order to solve the Navier Stokes equations numerically, the continuous variational problem (3.22 -3.24) must be transformed to a discrete variational problem. To find the finite element formulation we introduce the finite dimensional trial subspaces $V_h \subset V$ and $Q_h \subset Q$ and the finite dimensional test subspaces $\hat{V}_h \subset \hat{V}$ and $\hat{Q}_h \subset \hat{Q}$. The discrete variational problem reads: Find $u_h \in V_h \subset V$ such that

$$\begin{aligned}
a_1(u_h^*, u_h^{n-1}, p_h^{n-1}, v) =& L_1(f_h^n, v), && \forall v \in \hat{V}_h \subset V && (3.25) \\
a_2(p_h^n, q) =& L_2(p_h^{n-1}, u_h^*, q), && \forall q \in \hat{Q}_h \subset Q && (3.26) \\
a_3(u_h^n, v) =& L_3(u_h^*, p_h^n, p_h^{n-1}), && \forall v \in \hat{V}_h \subset V && (3.27)
\end{aligned}$$

where

$$\begin{aligned}
a_1(u_h^*, u_h^{n-1}, p_h^{n-1}, v) =& \langle v, \frac{u_h^* - u_h^{n-1}}{\Delta t} \rangle + \langle v, \nabla u_h^* \cdot u_h^{n-1} \rangle \\
&+ \langle \nabla v, \frac{1}{\rho} \sigma_h^n \rangle + \langle v, \frac{1}{\rho} p_h^{n-1} n \rangle_{\partial\Omega} \\
&- \langle v, \nu(\nabla u_h^* - \nabla u_h^{*T}) n \rangle_{\partial\Omega} && \forall v \in \hat{V}_h \subset V \\
L_1(f_h^n, v) =& \langle v, f^n \rangle && \forall v \in \hat{V}_h \subset V \\
a_2(p_h^n, q) =& \langle \nabla q, \nabla p_h^n \rangle && \forall q \in \hat{Q}_h \subset Q \\
L_2(p_h^{n-1}, u_h^*, q) =& \langle \nabla q, \nabla p_h^{n-1} \rangle - \frac{\rho}{\Delta t} \langle q, \nabla \cdot u_h^* \rangle && \forall q \in \hat{Q}_h \subset Q \\
a_3(u_h^n, v) =& \langle v, u_h^n \rangle && \forall v \in \hat{V}_h \subset V \\
L_3(u_h^*, p_h^n, p_h^{n-1}, v) =& \langle v, u_h^* \rangle - \frac{\Delta t}{\rho} \langle v, \nabla(p_h^n - p_h^{n-1}) \rangle && \forall v \in \hat{V}_h \subset V
\end{aligned}$$

The choice of $\hat{V}_h$, V_h, $\hat{Q}_h$ and Q_h arises from the type of finite elements that are applied to the problem. The Lagrangian element is well-suited for approximations in H^1 since it produces piecewise continuous polynomials. For our 3D problem, a simple but adequate choice is the linear Lagrange tetrahedron element with four nodes, one at each vertex. Hence, the subspaces $\hat{V}_h$, V_h, $\hat{Q}_h$ and Q_h are the spaces of all piecewise linear functions over a mesh of tetrahedrons.

The FEM-discretized IPCS-scheme is summarized in Table 3.2.

Table 3.2: The incremental pressure correction scheme (IPCS)

1. The tentative velocity $u*$ is computed by solving

$$\langle v, D_t^n u_h^* \rangle + \langle v, \nabla u_h^* \cdot u_h^{n-1} \rangle + \tfrac{1}{\rho}\langle \epsilon(v), \sigma(u_h^*, p_h^{n-1}) \rangle + \tfrac{1}{\rho}\langle v, p_h^{n-1} n \rangle_{\partial\Omega} - \langle v, \nu(\nabla u_h^*)^T n \rangle_{\partial\Omega}$$
$$= \langle v, f^n \rangle$$

where

$$D_t^n u_h^* = \tfrac{u_h^* - u_h^{n-1}}{\Delta t}$$

2. The corrected pressure p_h^n is computed by solving

$$\langle \nabla q, \nabla p_h^n \rangle = \langle \nabla q, \nabla p_h^{n-1} \rangle - \tfrac{\rho}{\Delta t}\langle q, \nabla \cdot u_h^* \rangle$$

including the inflow and outflow conditions for the pressure.

3. The corrected velocity u_h^n is computed by solving

$$\langle v, u_h^n \rangle = \langle v, u_h^* \rangle - \tfrac{\Delta t}{\rho}\langle v, \nabla(p_h^n - p_h^{n-1}) \rangle \quad \forall v \in V_h$$

The simulations are carried out in FEniCS, further described in Section 3.5. In order to solve a problem in FEniCS, it must be expressed as a variational problem and the space must be discretized with finite elements. The pre-written solver-program `ipcs.py` in the `nsbench`-directory (Logg et al, 2008, *https://launchpad.net/nsbench/*) implements the FEM-discretized Incremental Pressure Correction scheme for solving our problem.

We make adjustments to `solve()` -function in the `ipcs.py` - program to suit the discretization described above. The implicit discretization of the stress tensor σ and the semi-implicit discretization of the convection-term yields the modified expression for the tentative velocity step:

```
# Tentative velocity step
        F1 = (1/k)*inner(v, u - u0)*dx + inner(v, grad(u)*u0)*dx
             + inner(epsilon(v), sigma(u, p0, nu))*dx
             + inner(v,p0*n)*ds - beta*nu*inner(grad(u).T*n,v)*ds
```

```
            − inner(v, f)*dx
        a1 = lhs(F1)
        L1 = rhs(F1)
```

where k is the time-step and we assume that the pressure p is already scaled with the density ρ.

To improve performance speed, a modification to the vector function space V is made so that it is discretized by linear elements:

```
V = VectorFunctionSpace(mesh, "CG", 1)
```

The complete `solve()` - function with modifications follows.

```
    def solve(self, problem):

        if str(problem)=="Aneurysm":
            pc = "jacobi"
        else:
            pc = "ilu"

        # Get problem parameters
        mesh = problem.mesh
        dt, t, t_range = problem.timestep(problem)


        # Define function spaces
        V = VectorFunctionSpace(mesh, "CG", 1)
        Q = FunctionSpace(mesh, "CG", 1)
        DG = FunctionSpace(mesh, "DG", 0)

        # Get initial and boundary conditions
        u0, p0 = problem.initial_conditions(V, Q)
        bcu, bcp = problem.boundary_conditions(V, Q, t)

        # Remove boundary stress term is problem is periodic
        if is_periodic(bcp):
            beta = Constant(0)
        else:
            beta = Constant(1)

        # Test and trial functions
        v = TestFunction(V)
        q = TestFunction(Q)
        u = TrialFunction(V)
        p = TrialFunction(Q)
```

```
# Functions
u0 = interpolate(u0, V)
u1 = Function(V)
p0 = interpolate(p0, Q)
p1 = interpolate(p0, Q)
nu = Constant(problem.nu)
k  = Constant(dt)
f  = problem.f
n  = FacetNormal(mesh)

# Tentative velocity step
F1 = (1/k)*inner(v, u - u0)*dx + inner(v, grad(u)*u0)*dx
    + inner(epsilon(v), sigma(u, p0, nu))*dx
    + inner(v,p0*n)*ds - beta*nu*inner(grad(u).T*n,v)*ds
    - inner(v, f)*dx
a1 = lhs(F1)
L1 = rhs(F1)

# Pressure correction
a2 = inner(grad(q), grad(p))*dx
L2 = inner(grad(q), grad(p0))*dx - (1/k)*q*div(u1)*dx

# Velocity correction
a3 = inner(v, u)*dx
L3 = inner(v, u1)*dx - k*inner(v, grad(p1 - p0))*dx

# Assemble matrices
A1 = assemble(a1)
A2 = assemble(a2)
A3 = assemble(a3)

# Time loop

self.start_timing()
for t in t_range:

    # Get boundary conditions
    bcu, bcp = problem.boundary_conditions(V, Q, t)

    # Compute tentative velocity step
    b = assemble(L1)
    [bc.apply(A1, b) for bc in bcu]
    solve(A1, u1.vector(), b, "gmres", "ilu")

    # Pressure correction
    b = assemble(L2)
    if len(bcp) == 0 or is_periodic(bcp): normalize(b)
    [bc.apply(A2, b) for bc in bcp]
    if is_periodic(bcp):
        solve(A2, p1.vector(), b)
    else:
        solve(A2, p1.vector(), b, 'gmres', 'amg_hypre')
    if len(bcp)==0 or is_periodic(bcp):normalize(p1.
        vector())
```

```
            # Velocity correction
            b = assemble(L3)
            [bc.apply(A3, b) for bc in bcu]
            solve(A3, u1.vector(), b, "gmres", pc)

            # Update
            self.update(problem, t, u1, p1)
            u0.assign(u1)
            p0.assign(p1)

        return u1, p1
```

3.2 Model generation in VMTK

For our simulations we reconstruct patient-specific anatomy of the cerebrospinal fluid system in both Chiari-patients and healthy volunteers. Starting off with MRI-scans of a person's lower posterior fossa and cervical portion of the spine, we extract the CSF-canal and create a corresponding 3D model which can later be used for our simulations. For this purpose we use the Vascular Modeling Toolkit (VMTK), which is a software tool for generation of 3D models of different anatomical structures, most commonly used for reconstruction of blood vessels (*http://www.vmtk.org*). The reconstruction is based on segmentation; a process of locating objects and boundaries in images, which in this case are MRI-scans of a patient. The different methods we mention below are further described on the VMTK website.

3.2.1 Image segmentation

To be able to compare velocities at the same anatomical levels, we choose to segment the exact same parts of the anatomical regions in all of the patients and the volunteers. Because of the complexity of the anatomy higher up, all of the models start just above the level of the foramen magnum, at the tip of the occipital bone. Since the quality of the MRI-scans for many of the patients decreases below C5, segmenting these images further would put the credibility of the models to question. For this reason, all of the models end at this level. The physical length of this extracted region varies from patient to patient, resulting in models of varying lengths.

Starting off with DICOM directories consisting of an MRI-scan of a patient or a volunteer, we read these directories into VMTK to visualize the anatomy. In Figure 3.1 we can see an anatomy with Chiari malformation clearly visible as the tonsils exceed down into the CSF-spaces. Since we are only interested in reconstructing a small part of this anatomy, we use the `vmtkimagevoiselector` to extract the volume of interest(VOI).

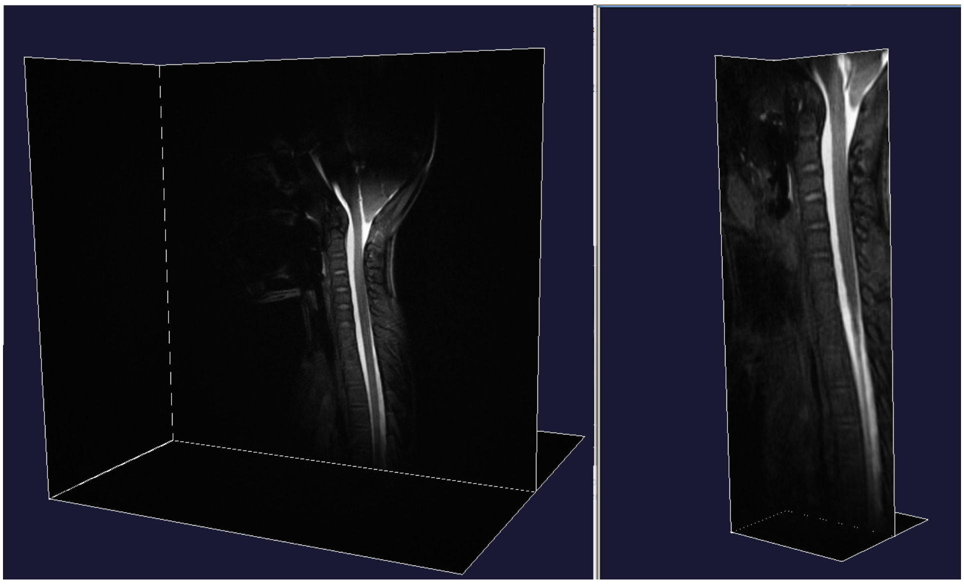

Figure 3.1: *MRI-scan of a person with the Chiari Malformation (left) and the extracted volume of interest which we use for model creation(right).*

The selected volume of interest is then segmented in VMTK. As a segmentation tool, VMTK uses the level sets method which is a numerical technique for shape-tracing. This method represents shapes with the help of a function; the level set function. The shape is described by the contour of this function at level zero.

For initialization of the model, we call `vmtklevelsetsegmentation -ifile [input_file].vti -ofile [output_file].vti` , where input file is the extracted VOI and the output file is where the segmentation will be saved. The user is then prompted to choose from a list of level set methods. We use the colliding fronts-method as it proves most convenient and effective in extracting the CSF-channel. This method consists of placing two seeds on the image. Figure 3.2 illustrates this procedure. The CSF-fluid in the MR-pictures has a lighter color than the rest of the surrounding anatomy. The user places both seeds in the location of the fluid, in a reasonable distance from each other. VMTK propagates a front from each of the seeds, in the direction of the other seed. The two fronts omit regions with intensity that differs considerably from the intensity in the seeds' location. Thus, the fronts trace the shape of the fluid's path. The region where the fronts cross makes up the segmented piece of the CSF-pathway.

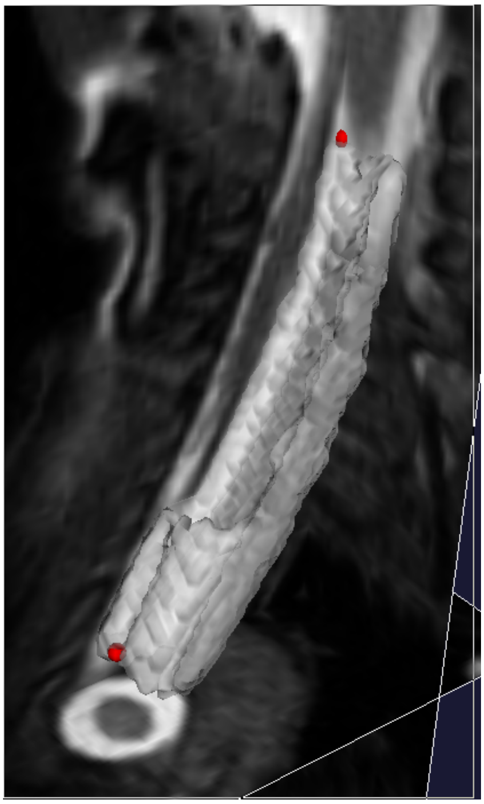

Figure 3.2: *A part of the CSF-pathway traced by the colliding fronts.*

The models are made by continuous repetition of the colliding-fronts method combined with appropriate thresholding. Due to inhomogeneities in the magnetic fields, darkening of the signal intensity toward the lower end of the spine occurs. Additionally, the differences in intensity tend to get smaller in these parts of the MRI-image. This often results in failure of the colliding fronts method alone, as it segments the surrounding anatomy together with the CSF. To maintain the correctness of the segmentation, thresholding is used together with the colliding fronts method. Since the CSF-pathway has higher pixel-values than the rest of the surrounding anatomy, we specify an appropriate maximum threshold value so that the darker regions are omitted by the colliding fronts and are not made part of the model. The specified thresholds are continuously adjusted according to the changing image intensities. The resulting segmentations are merged into one.

3.2.2 Adjustments to the segmentation process

A range of adjustments to the segmentation process are made during the level set segmentation in the different cases mentioned below. These editions will influence our models to such minor degree that our results are assumed left unchanged.

Manual segmentation using single seeds

Option `-seed` in the level set method is chosen to segment parts of the model where for different reasons the colliding fronts method does not succeed (Figure 3.3). This often occurs in regions where the walls of the SAS are very narrow, leading to small intensity-variations not detected by the colliding fronts. The segmented walls are further made thinner by deformation steps performed after the level sets method.

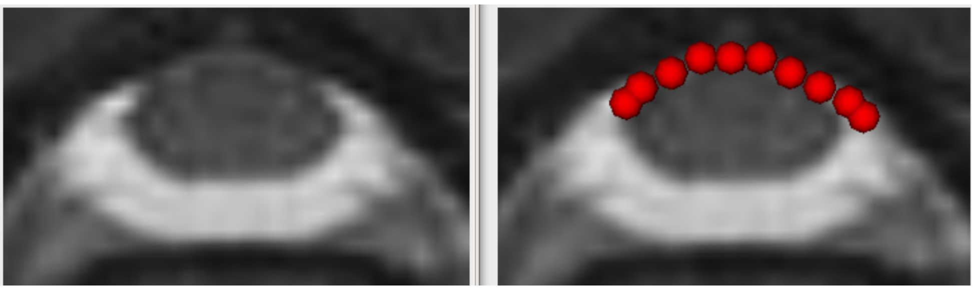

Figure 3.3: *Thin canal walls (left) and individual seeds used to segment them (right).*

The segmentation is done manually, using individual seeds, in cases where the contrast in the image is too poor for the colliding fronts method and thresholding to succeed (Figure 3.4). This happens mainly in lower parts of the spine. A disadvantage is that the resulting segmentation is highly dependent on visual evaluation of the images which might result in erroneous outcomes. However, manual segmentation is kept to a minimum, only adopted in very small parts of the model, and if really necessary. Often, the successfully segmented parts of the image clearly mark the shape of the SAS and the seeds are used to fill up the holes in the model which have not been segmented. Manual segmentation may also result in a slightly edgy surface of the segmented model parts. However, after the deformation and smoothing procedures these effects are significantly diminished.

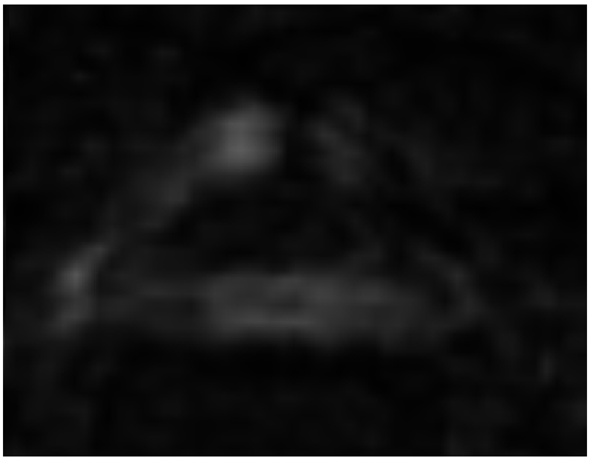

Figure 3.4: *Decreased contrast in the lower parts of the MRI-scan.*

Blood vessels

In most of the anatomies, there are blood-vessels inside the CSF canal (Figure 3.5) which are omitted by the level set segmentation. This leads to creation of empty canals inside the model, making it impossible for VMTK to generate a mesh. Because of their thinness, we assume that these vessels do not have a big influence on the CSF-flow. Hence, they are segmented as a part of the CSF, using either individual seeds or the colliding fronts method.

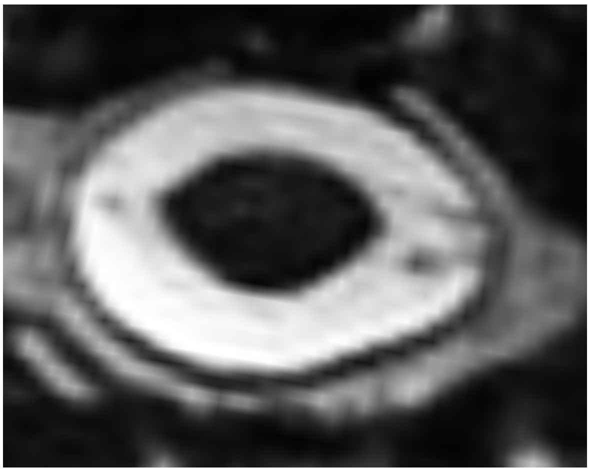

Figure 3.5: *Blood-vessels inside the CSF-canal.*

Tonsils

VMTK can only handle mesh-generation of the segmented surfaces if the model is fairly cylindrical - shaped. This leads to obstacles just below foramen magnum where the tonsils extend into the CSF-canal Figure 3.6 illustrates the anatomy together with the generated model. Segmenting the CSF behind the tonsils, produces a surface with additional opening at the top, making it difficult for VMTK to generate a mesh. Hence, we choose not to segment the CSF behind the tonsils, assuming that it makes such small part of the CSF volume, it will not make much difference in the simulations.

Figure 3.6: *The small part of the CSF behind the extended tonsils is not segmented.*

Special cases

In two of the patients some unexpected characteristics occur in the anatomy. In one patient (Figure 3.7), there is a black spot on the MRI-scans just below the foramen magnum. The spot is assumed to be a lump of fat which has an impact on the CSF-flow. This lump is hence not segmented as part of the CSF.

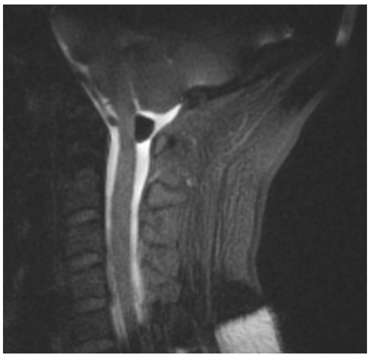

Figure 3.7: *Patient no.11.*

In another patient who has been operated ahead of the MRI-scan a long cylinder-shaped vessel can be seen on the images (Figure 3.8). Since its shape and thickness is similar to that of a blood-vessel, it is segmented as a part of the CSF-canal.

Figure 3.8: *Patient no.18: the axial and sagittal view.*

3.2.3 Smoothing and clipping

The result of the level set segmentation is an image, which zero-level is the surface in question. We extract this surface using `vmtkmarchingcubes`. Figure 3.9 (left) illustrates the result.

The extracted surface is smoothed with passband 0.1 which eliminates some high frequency irregularity in the surface and at the same time produces minimal model shrinkage. The ends of the surface are clipped using the

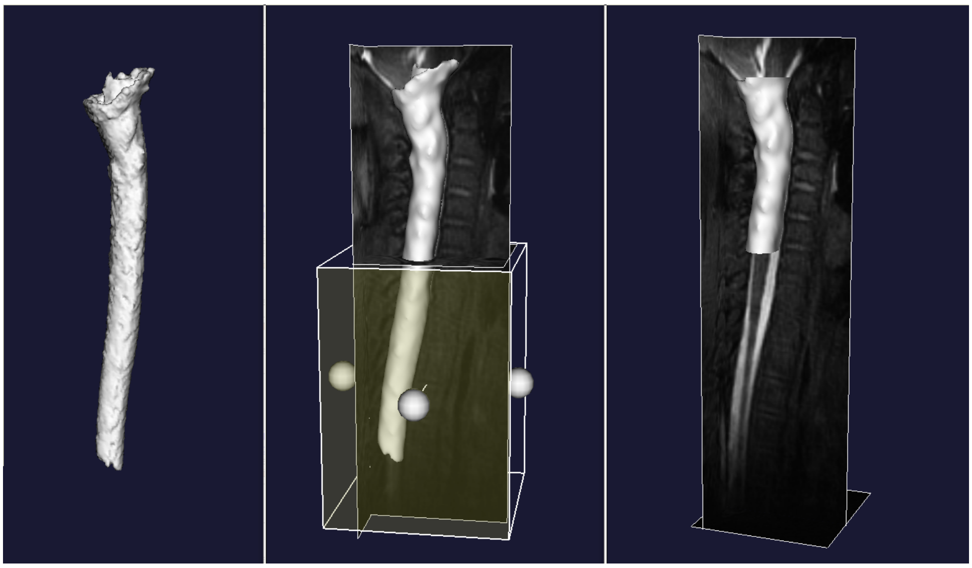

Figure 3.9: *The surface extracted using the marching cubes-method (left), the clipping of the smoothed surface(middle) and the surface after clipping (right).*

`vmtksurfaceclipper`. Applying `vmtkrenderer`, we visualize the vertebral column in the MR images while performing the clipping at the foramen magnum and above C6. The picture in the middle of Figure 3.9 illustrates this procedure. The surface inside the transparent polygon in the picture is clipped away. The user adjusts the size and the location of this polygon before conducting the clipping.

3.2.4 Resolution-control

Generating the mesh with cells of the default edge-length 1.0, results in the narrow regions in the modelled SAS having only one or two cells in width. This leads to unwanted effects during simulation, e.g. because of the no-slip condition where the outer cells are assigned zero velocity. We control the resolution of those narrow parts of the model using the `vmtkdistancetospheres` -script (Morvan, 2009).

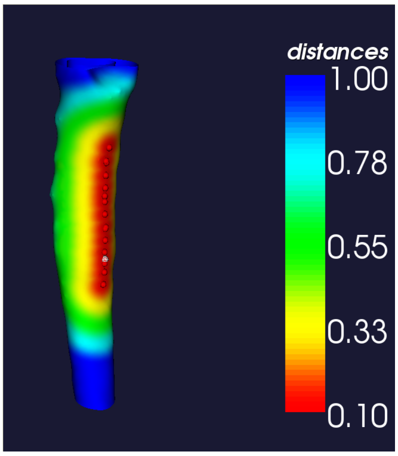

Figure 3.10: *Controlling mesh resolution.*

The procedure consists of placing seed points in locations where the walls of the model are thin (Figure 3.10). We then specify an array which controls the edge length of the cells in the area around these seeds. In the model in Figure 3.10, the smallest edge-length is chosen to be 0.1 mm, the largest edge-length is 1.0 mm.

3.2.5 Mesh generation

The `vmtkmeshgenerator` creates a mesh from the segmented and edited surface. The option `-cappingmethod annular` is specified for the capping at the inflow and the outflow boundaries of the model to be correct. The resulting mesh is made up of triangular-shaped cells. It is converted from the original vtu-format to the xml-format accepted by DOLFIN using `vmtkmeshwriter`.

3.3 Pre-processing of the MRI-images in ImageJ

Two of the patients have large syrinxes inside their spinal canals. The syrinxes in the MRI-scans have the same pixel-intensity as the CSF. The border between the CSF and the syrinx is often fairly unclear (see Figure 3.11). Straightforward segmentation using the level sets is thus not possible, since the colliding fronts do not exclude the syrinx and segment it as part of the CSF-spaces. Pre-processing the image in order to hide the syrinx is therefore necessary. For this purpose, we apply ImageJ.

ImageJ (*http://rsb.info.nih.gov/ij/*) is a freely available image processing toolkit. It can read many image formats including TIFF, PNG, GIF, JPEG, BMP, DICOM and raw formats. It can be used for image analysis, editing or image processing operations such as logical and arithmetical operations between images, contrast manipulation, convolution, Fourier analysis, sharpening, smoothing and edge detection. More information about the toolkit can be found on the ImageJ website.

ImageJ makes it is easy to upload and edit a stack of related images at the same time. It is hence a useful tool for editing DICOM - pictures. We upload the whole DICOM-directory with MRI-images of the patient by choosing the option `Import - Image Sequence` . It is then possible to scroll between the different images and make adjustments to them. In the toolbox, we find the color-picker tool. With this tool, we click on the image-location with the desired color-intensity to assign to the syrinx. We choose a darker color in order to separate the syrinx from the CSF. Next, we find the paintbrush tool. Right-clicking on it, we choose an appropriate brush-width, in pixels. The syrinx in every image is then colored darker (Figure

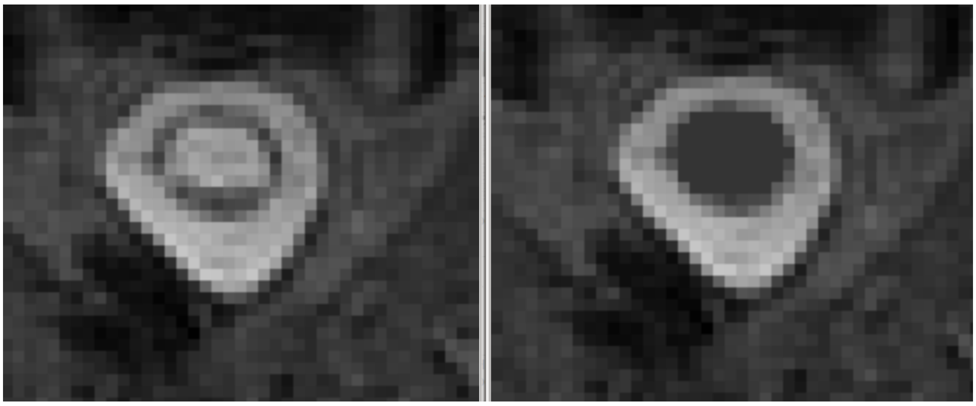

Figure 3.11: *Spinal canal with syrinx (left). The syrinx is colored darker using ImageJ (right).*

3.11). This way, the level set method conducted on the image segments only the high-intensity CSF-fluid surrounding the cord and the syrinx is left out from the model.

3.4 Boundary marking in Meshbuilder

FEniCS Meshbuilder is a tool for marking boundaries on models which will be used for numerical simulations. The mesh of the CSF-canal is loaded into the Meshbuilder in the xml-format generated by the VMTK. The inflow, outflow and no-slip boundaries of the mesh are easily marked (Figure 3.12).

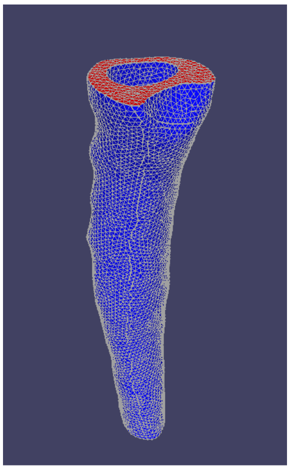

Figure 3.12: *A model of the CSF-canal with indicated inflow-boundary (red) and no-slip boundary (blue).*

3.5 Simulations in FEniCS

For conduction of simulations on the models of the CSF-canal, we use FEniCS (*http://www.fenicsproject.com*). *The FEniCS Project is a collection of free software aimed at automated, efficient solution of differential equations. The project provides tools for working with computational meshes, finite element variational formulations of PDEs, ODE solvers and linear algebra.*

FEniCS programs are written in Python programming language. One of the strengths of FEniCS is that there is a close correspondence between the mathematical formulas and how they are expressed with the Python syntax. This makes FEniCS very easy to use. The key classes in a FEniCS program are being imported from the DOLFIN software library which consists of C++ classes for finite element calculation, for instance classes for boundary conditions Dirichlet, Neuman etc.

For our implementation we use the pre-written programs found in the `nsbench` - directory (Logg et al, 2008). Here, the main script `ns` allows the user to solve a chosen problem with a given solver. In our case, we use the problem-script `channel.py` together with the solver-script `ipcs.py`. We make small adjustments to both of the scripts in order to match our criteria. Adjustments to `ipcs.py` have already been described in Section 3.1.

In `channel.py` we implement the problem by defining its parameters, the mesh and the initial and boundary conditions. The mesh used in the simulations is read from file constructed beforehand with the VMTK. The appropriate viscosity is defined (see Table 3.1). Body forces are assumed negligible and are set to zero. The end time is set to 5 s along with the time step $dt = 0.005s$.

```python
# Problem definition
class Problem(ProblemBase):
    "3D␣Chiari␣problem."

    def __init__(self, options):
        ProblemBase.__init__(self, options)

        # Upload mesh
        self.mesh1 = Mesh('patient_1.xml')

        #Scale mesh from mm to cm
        for coor in self.mesh1.coordinates():
            coor[0]=coor[0]/10.0
            coor[1]=coor[1]/10.0
            coor[2]=coor[2]/10.0

        #Set top-bottom z-coordinates of the mesh
        self.z_max = 16.58
        self.z_min = 22.08
```

```
        # Body force assumed to be zero
        self.f = Constant((0, 0, 0))

        # Set viscosity
        self.nu =  0.7*10**-2           #(cm2/s)

        # Set end-time
        self.T = 5.0                    #s

        #Set max u
        self.U = 15                     #cm/s

        #Set time-step
        self.dt = 0.005                 #s
```

For the initial condition, the pressure and the velocity are set to zero.

```
    def initial_conditions(self, V, Q):
        u0 = Constant((0, 0, 0))
        p0 = Constant(0)
        self.pressure_function = p0
        return u0, p0
```

The boundary indicators are read from files created in FEniCS Meshbuilder. Using the DOLFIN-class `DirichletBC`, the inflow, outflow and no-slip boundary conditions are easily assigned.

```
    def boundary_conditions(self, V, Q, t):
        # Upload boundary-markers:
        inflow_boundary = 'patient_1_inflow_boundary.xml'
        outflow_boundary = 'patient_1_outflow_boundary.xml'
        noslip_boundary = 'patient_1_no_slip_boundary.xml'

        self.sub_domain_no_slip =  MeshFunction("uint", self.
            mesh, noslip_boundary)
        self.sub_domain_inflow =  MeshFunction("uint", self.mesh
            , inflow_boundary)
        self.sub_domain_outflow =  MeshFunction("uint", self.
            mesh, outflow_boundary)

        # Create no-slip boundary condition for velocity
        bv = DirichletBC(V, Constant((0.0, 0.0, 0.0)), self.
            sub_domain_no_slip, 3)

        # Create boundary conditions for pressure
        bp0 = DirichletBC(Q, self.pressure_bc(Q,t), self.
            sub_domain_inflow, 1)
        bp1 = DirichletBC(Q, self.pressure_bc(Q,t), self.
            sub_domain_outflow, 2)

        bcu = [bv]
        bcp = [bp0, bp1]
```

```
        return bcu, bcp
```

The pressure function is specified in a separate function in the program.

```
    def pressure_bc(self, Q,t):

        #Set max pressure gradient to 24.3 Pa/density
        b = 2.43*10**2

        #Set max pressure to 1961.33 Pa/density
        c = 1.96*10**4
        element = FiniteElement("CG", triangle, 1)
        pii = dolfin.pi
        a = Expression("(c-b*(zmax-x[2])/(zmax-zmin))*sin(2*pii*
            t)", element=element)
        a.b = b
        a.c = c
        a.t = t
        a.pii = pii
        a.zmax=self.z_max
        a.zmin=self.z_min
        self.pressure_function = a
        return a
```

3.6 Analysis in ParaView

ParaView (*http://www.paraview.org*) is a visualization tool which we use for examination of the models and the simulation results. It supports a variety of file formats and can visualize the data interactively in 3D. Paraview has many useful tools that improve the data analysis and visualization. A complete description of its features can be found on the Paraview website.

3.6.1 Analysing mesh-resolution

The models created in VMTK are uploaded in Paraview for inspection. By applying the clipping tool, a model is cut with an arbitrary plane to analyze the thickness of its walls. This is helpful in investigating which parts of the model have narrow walls and deciding what edge-lengths should be assigned to these segments.

3.6.2 Visualizing the results

Animations of the simulation results are visualized in Paraview. We choose to show the results at six different horizontal levels of the anatomy. We extract those parts of the surface using the slicing tool. The corresponding MRI-images are uploaded in order to visualize the surrounding anatomy together with the model. This makes it easy to extract the same levels of the anatomy in all of the patients. Figure 3.13 (left) depicts the sagittal view of the anatomy together with the axial levels which we choose to extract. The first slice is on the level of the foramen magnum, just below the occipital bone. The second slice is taken at the level of C1/C2, the third above C3, the fourth above C4 and the fifth above C5. The last slice is taken just above the level of C6. Additionally, there is one slice taken along the sagittal plane. This plane, when viewed from above, runs approximately through the mid-line of the model.

Velocities in the simulations are visualized using color plots (Figure 3.13 (right)). The plots have a blue-white-red color-range where red depicts the highest velocity. The user chooses to visualize either the velocity magnitudes or a single component of the velocity. Viewing just the z-components is useful when finding bidirectional flow. Yet another helpful tool is Glyph, which is used to visualize the vector field of the points in the dataset. Paraview provides the possibility to upload more models together, to compare the results of simulations on different patients.

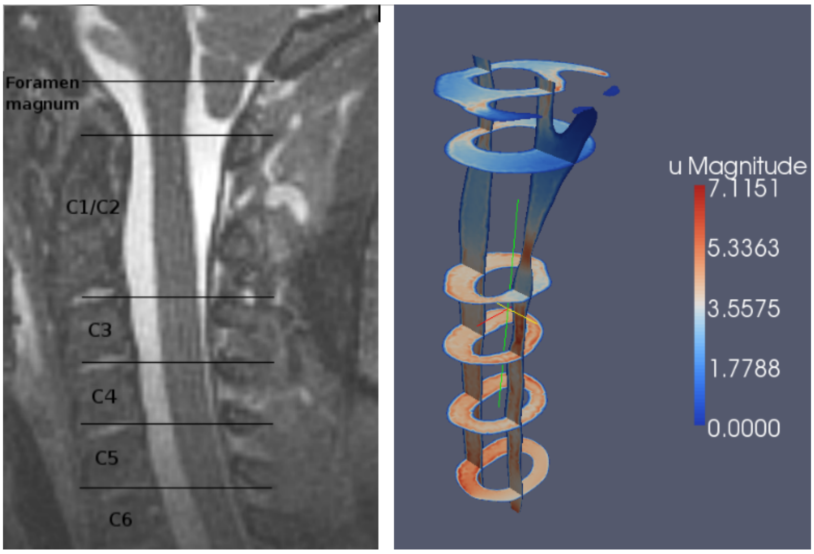

Figure 3.13: *Axial levels at which we choose to extract the data (left). The velocities at the extracted levels visualized in Paraview (right). It should be noted that the MR image to the left is not of the modelled patient to the right.*

3.7 Outline for result analysis

3.7.1 Tapering

For all the models, we conduct area measurements of the SAS at five different axial levels of the anatomy. The following code computes the area at the level of C1 for one patient. The location of C1 is found beforehand in Paraview.

```
class C1(Expression):
    def eval(self, values, x):
        if x[2] >= 209 and x[2] < 219:
            values[0] = 1.0
        else:
            values[0] =  0.0

c1 = C1()
area_c1 = (assemble(c1*dx, mesh=self.mesh))/10
```

The area is found similarly for all the evenly distributed five axial levels between C1 and C5. From these five measurements, we compute the average area for each model. Finally, we compute deviation from the average area at each level.

3.7.2 Pressure distribution inside the models

To inspect how the pressures are distributed inside the models, we measure pressure at six different levels between the top and the bottom. The measurements are made at the time of maximum systolic pressure gradient.

3.7.3 Finding peak velocities

In order to eliminate possible influence of the inflow and outflow boundary conditions, we clip away a small part of the top and the bottom of the model. Highlighting the clipped model in Paraview and choosing, "Rescale to data-range", yields the maximum velocity at a given time. Peak systolic velocities are found halfway through the simulated cardiac cycle, while peak diastolic velocities are found at the end of the cycle.

3.7.4 Studying velocity patterns

Velocity patterns are found by visual inspection of the models. Paraview gives the possibility to upload more models together in order to study similarities and differences between them. Since the models have different positions in space, we use the transform-filter to line-up the models next to each other. The slice-tool gives the possibility to extract a chosen part of the model along a selected axis. It is thus possible to e.g. compare velocity patterns along the sagittal or axial lines.

In this study, jets are identified by reference to the color plots of CSF velocities. When velocities in one region of the subarachnoid space exceed those in the adjacent region by more than 100%, the region is classified as a jet.

3.7.5 Synchronous bidirectional flow

Magnitudes of the z- velocity component are analyzed for each model. Flow where velocities larger than 0.1 cm/s occur in both z-directions simultaneously is considered as bidirectional. In this study, we denote the maximum bidirectional flow difference to be the maximum difference between caudad and cephalad velocities that occur at the same axial level. The level at which the synchronous bidirectional flow visually seems to have the biggest magnitude is extracted. The maximum difference in velocities is found by parsing through the time-steps.

3.7.6 Flux

Flux is the amount of fluid that flows through a given area per unit time. In our case, flux depends on the size of the surface, magnitude of velocity and the normal n which is referred to as facet normal in FEniCS. We compute flux at the top and at the bottom of each model. This is done by restricting the computation to inflow and outflow parts of the boundary which are marked in Meshbuilder. Flux is measured for every time-step. Maximal flux is found for all the patients. It should be noted that the flux is equal at the top and at the bottom of the model but it is computed at both ends to check the correctness of the simulations.

```
def flux(self, i, u):
        n = FacetNormal(self.mesh)
        flux_ = dot(u, n)*ds(i)

        #Top boundary corresponds to subdomain no. 1
        if i==1:
                a = assemble(flux_, exterior_facet_domains=
                    self.sub_domain_inflow, mesh=self.mesh)

        #Bottom boundary corresponds to subdomain no. 2
        elif i==2:
                a = assemble(flux_, exterior_facet_domains=
```

```
                    self.sub_domain_outflow, mesh=self.mesh)
        return a

flux_top = flux(1,u)
flux_bottom = flux(2,u)
```

At each time-step, the flux magnitude is stored in a file for each of the patients respectively. Letting $Q(t)$ denote the flux at the top of the model at time t, we compute the total amount of fluid in ml that flows through the model during one cardiac cycle ($\frac{\int |Q(t)|\, dt}{2}$), the total change in flux $\int |Q'(t)|\, dt$ as well as the ratio $\frac{\int |Q'(t)|\, dt}{\int |Q(t)|\, dt}$ which describes the pulsation of the fluid in relation to the total flow volume.

3.7.7 Student t-test

Due to varying standard deviations of the three groups, comparing just the averages of the results for each group separately might not give a sufficient impression of the differences between them. Hence, a student t-test (e.g. Løvås, (2004)), is conducted in order to give an additional indication if there are significant differences between Chiari I patients, volunteers and postoperative patients. T-test is the most common method to compare data between two groups. In this study, the type of t-test is unpaired, as the data in the compared groups are assumed to be independent of each other.

The essence of a t-test is to define a null-hypothesis, which usually states that there is no difference between the two studied groups. Further, the null-hypothesis is rejected if the P-value returned by the t-test is lower than a chosen significance level-value. $P = 0.05$ is a common significance level which we will employ in this study. Two-tailed t-test is applied to inspect if there is a difference between two groups, in either direction. One-tailed t-test is applied if we have a directional hypothesis, e. g. if we suspect that one of the groups has higher values than the other.

The t-test is conducted using the `TTEST` -function incorporated in the OpenOffice.org Spreadsheet - package (*http://www.openoffice.org/*) Assuming that the data to be compared are defined in two separate arrays (`data1`) and (`data2`), the syntax for t-test in OppenOffice.org is the following:

```
TTEST(data1; data2; mode; type)
```

where mode defines if the test is one-tailed (`mode=1`) or two tailed (`mode=2`) while `type=3` as the samples are assumed to have unequal variance. The

P-value returned by the t-test is compared against the chosen significance level and the null-hypothesis is accepted or rejected accordingly.

By utilizing an unpaired t-test we assume that the sample distribution is normal. However, it should be noted that with the small sample size in this study, this assumption cannot be clearly justified. Thus, the t-test is applied only as an additional indication to our findings and our conclusions are not based on its results.

3.8 Method-tests

3.8.1 Testing cycle repeatability

In order to check how fast a steady state is reached, peak velocities are compared for the fourth and fifth cycle at four points in time: $t = 0.0s$, $t = 0.25s$, $t = 0.5s$ and $t = 0.75s$. Table 3.3 shows the results. We observe that even after five cardiac cycles the flow is not fully stabilized especially at time of peak systolic flow, where the differences are 6.0%. Figure 3.14 shows the maximum velocity magnitudes at six axial levels at $t = 0.5s$ during the 4th and the 5th cycle. We observe equal velocity patterns in both cycles. We consider the results from the 5th cycle satisfactory, thus, all the results presented below are taken from the 5th cardiac cycle.

Table 3.3: Peak velocities in 4th and 5th cardiac cycle

Time (s)	4th cycle	5th cycle	Difference
0.0	10.9 cm/s	11.2 cm/s	2.7%
0.25	6.5 cm/s	6.4 cm/s	1.5%
0.5	13.3 cm/s	12.5 cm/s	6.0%
0.75	6.2 cm/s	6.3 cm/s	1.6%

3.8.2 Time-step test

Simulations with different time-steps are conducted on one of the models in order to check if the result are influenced by the size of the time-step. Table 3.4 shows comparison of maximum velocities at four times during the cardiac cycle for simulations with $\Delta t = 0.001$ and $\Delta t = 0.005$ on the same model. We see that at times of peak diastolic and peak systolic flow, the differences are minimal. The largest difference occurs at $t = 0.75s$. We choose to consider $dt = 0.005$ a satisfying time-step, hence, all the results presented below are obtained with $dt = 0.005$.

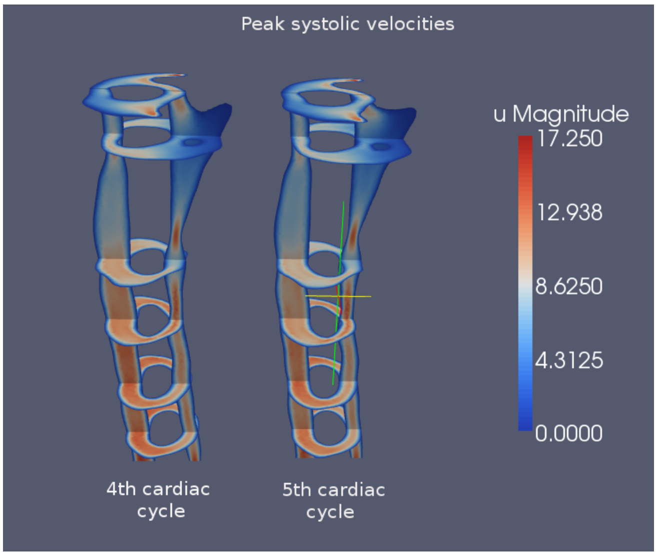

Figure 3.14: *Velocities at $t = 0.5s$ during the 4th and the 5th cardiac cycle*

Table 3.4: Peak velocities with different time-steps

Time (s)	$dt = 0.001$	$dt = 0.005$	Difference
0.00	10.70 cm/s	10.44 cm/s	0.2%
0.25	6.59 cm/s	6.41 cm/s	2.8%
0.50	14.39 cm/s	14.35 cm/s	0.3%
0.75	5.99 cm/s	5.6 cm/s	6.7%

3.8.3 Resolution test

A simulation on a model with more than three times as many cells as original is conducted. Table 3.5 shows maximum velocities at four time-steps in the cardiac cycle. The differences between the two models are most visible during time of flow reversal. Figure 3.15 shows the two models at time $t = 0.5\ s$. We observe that the velocity-patterns look approximately the same in both cases.

Table 3.5: Resolution test: Comparison of maximum velocities

Time	Coarser grid	Finer grid	Difference
$0.0s$	$11.45cm/s$	$11.37cm/s$	0.7%
$0.25s$	$5.86cm/s$	$6.27cm/s$	6.7%
$0.5s$	$12.48cm/s$	$12.26cm/s$	1.8%
$0.75s$	$5.79cm/s$	$6.21cm/s$	7.0%

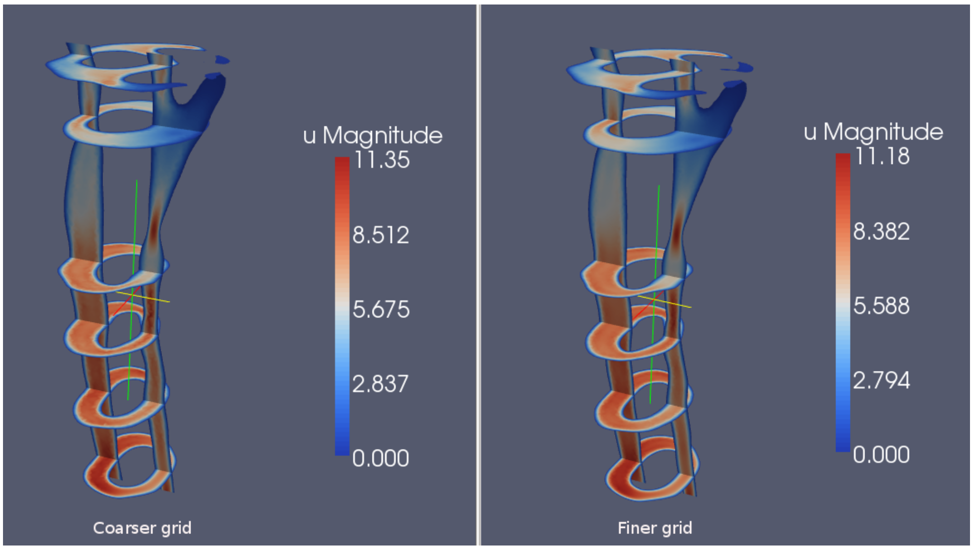

Figure 3.15: *Peak systolic velocities in a mesh with 550 K cells (left) and in the same mesh with 1900K cells (right).*

3.8.4 Uneven pressure gradient

The pressure is set so that at its peak, the pressure gradient posterior to the cord has 20% higher magnitude than the pressure gradient anterior to the cord. The goal is to check if uneven pressure values at one of the boundaries has a significant impact on the pressure-distribution inside the model and on the velocities of the fluid. Figure 3.16 shows the pressure distribution inside the model with uneven pressure gradient (left) and in the original model (right). We observe that the differences in pressure distribution are clear at the top of the model.

To inspect difference in pressure distribution, we extract eight axial levels in the model, evenly distributed between the top and the bottom. Table 3.6 shows the comparison of pressure distributions at each level. We observe that with the pressure values 20% higher posterior to the cord at the foramen magnum-level, the differences at the remaining levels are minimal.

Pressure distribution inside the model

Level	1(Top)	2	3	4	5	6	7	8(Bottom)
Even grad. (Pa)	1960	1957	1955	1952	1948	1944	1940	1936
Uneven grad. (Pa)	1960 – 1921	1955	1953	1950	1947	1944	1940	1936
Difference (%)	0 – 20	0.1	0.2	0.2	0.01	0	0	0

Table 3.6: *Comparing pressure distributions at different axial levels*

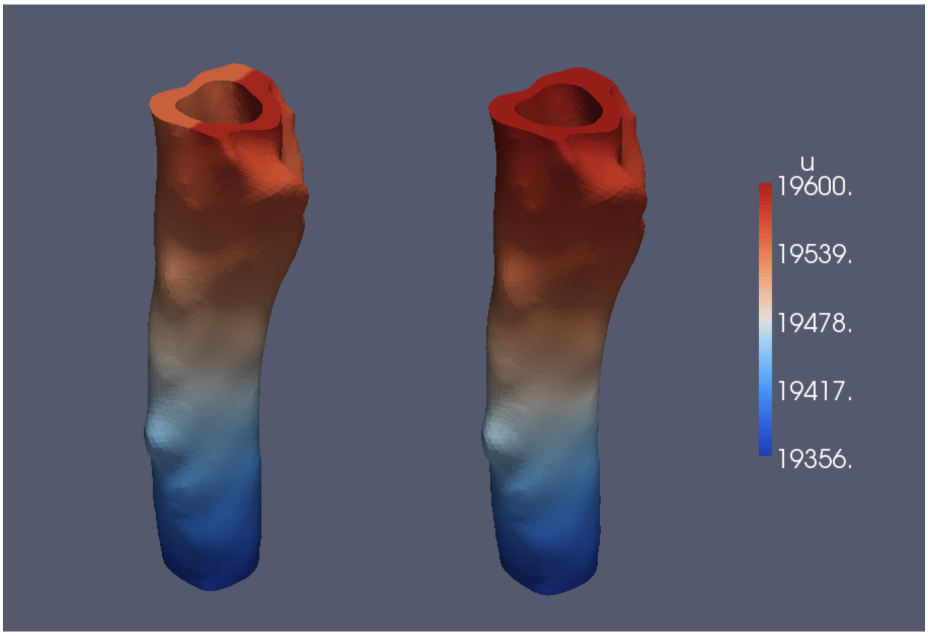

Figure 3.16: *Pressure distribution with uneven pressure gradient (left) and even gradient (right) set at the top of the model.*

Table 3.7 shows difference in peak systolic velocities at six different axial levels in the anatomy. We observe that, apart from at foramen magnum, the velocities differ minimally. We note that the differences, although minimal, are greater towards the bottom of the model than at the levels of C2-C4.

Table 3.7: Comparison of velocities at different axial levels

Level	Test p	Normal p	Difference
FM	$10.3cm/s$	$22.5cm/s$	74.4%
C2	$7.3cm/s$	$7.3cm/s$	0%
C3	$8.8cm/s$	$8.8cm/s$	0%
C4	$9.6cm/s$	$9.5cm/s$	1%
C5	$8.9cm/s$	$9.3cm/s$	4.4%
C6	$10.6cm/s$	$10.1cm/s$	4.8%

3.8.5 Asymmetric pressure function

To check the outcomes of a different flow pulse, a simulation with an asymmetric pressure function (e.g. Logg et al. (2010)) is conducted on one of the models. Figure 3.17 shows a plot of the pressure difference between the top and the bottom of the model resulting from the asymmetric flow pulse and the symmetric flow pulse respectively.

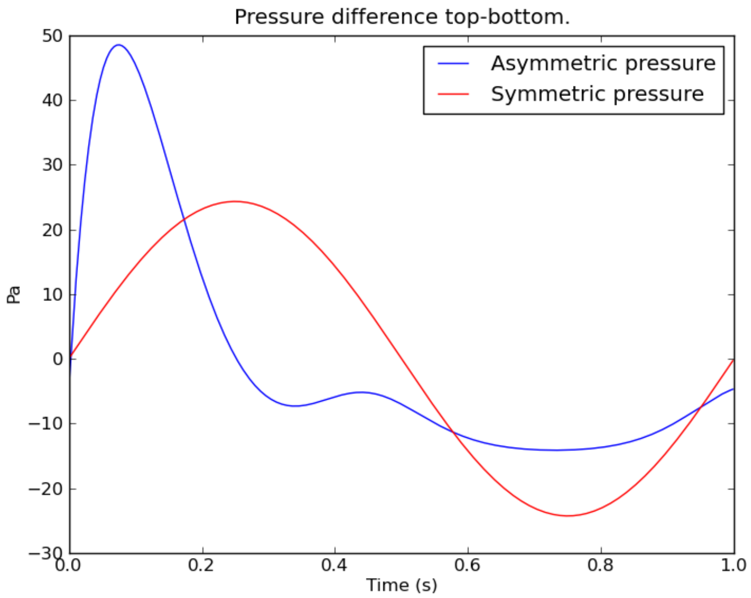

Figure 3.17: *The asymmetric and the symmetric pressure functions.*

Table 3.8 shows a comparison of different flow characteristics in the same model with applied asymmetric and symmetric pressure function, respectively. We note that the differences are fairly small.

Table 3.8: Comparison of flow characteristics

Flow characteristic	Asymmetric p	Symmetric p	Difference
Peak systolic v (cm/s)	13.5	13.5	0%
Peak diastolic v (cm/s)	12.6	13.0	3.1%
Max bidirectional flow difference (cm/s)	$6,9$	7.2	4.2%
Bidirectional flow duration (s)	0.2	0.2	0%
Max flux (cm^3/s)	5.3	5.8	9%

Chapter 4

Results

4.1 Geometric models

The generated models are of different sizes, as the modelled patients and volunteers are of different ages. Table 4.1 contains information on MRI-measurements of tonsil extensions below foramen magnum, gender and age of the modelled patients and whether they have syrinxes in their spinal canals.

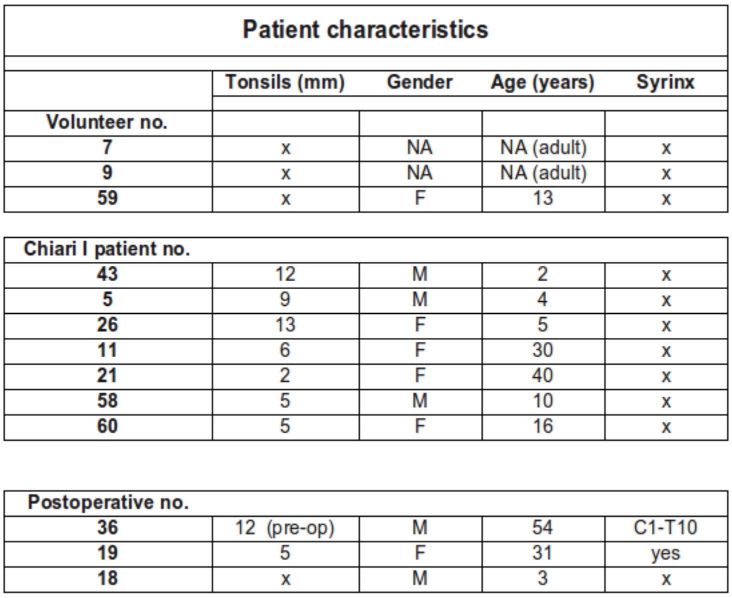

Patient characteristics

	Tonsils (mm)	Gender	Age (years)	Syrinx
Volunteer no.				
7	x	NA	NA (adult)	x
9	x	NA	NA (adult)	x
59	x	F	13	x
Chiari I patient no.				
43	12	M	2	x
5	9	M	4	x
26	13	F	5	x
11	6	F	30	x
21	2	F	40	x
58	5	M	10	x
60	5	F	16	x
Postoperative no.				
36	12 (pre-op)	M	54	C1-T10
19	5	F	31	yes
18	x	M	3	x

Table 4.1: *Explanation of the symbols: M=male, F=female, NA = not available, x = not present (syrinx)/ not herniated (tonsils), pre-op = measured prior to surgery, C1-T10 - length of the syrinx.*

It should be noted that tonsil extensions in some of the generated models are of slightly different length than the ones measured beforehand in the MRI images. Tonsils are clearly visible in two of the postoperative models and slightly visible in one of the healthy models.

Table 4.2 gives the length and the information on tapering for each model. The length denotes the distance between the top and the bottom of a model in z-direction. However, we note that some of the models are more curved in shape and thus their length differs slightly from the one computed in the z-direction. The sizes of the resulting meshes range between $7.0 \cdot 10^5$ and $3.0 \cdot 10^6$ cells, which requires significant computational time for the simulations.

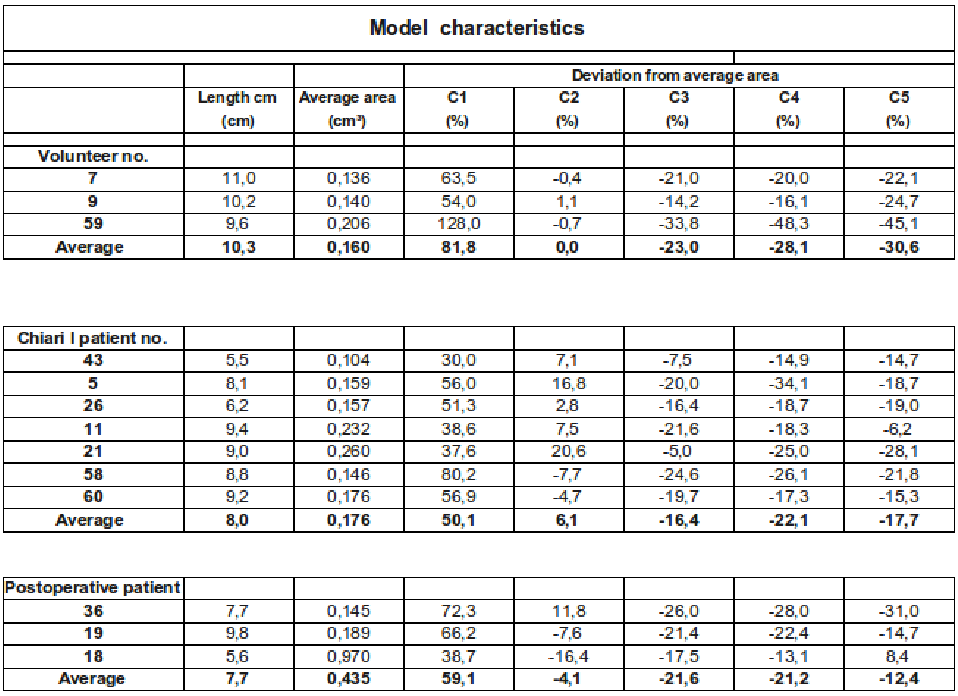

Model characteristics

	Length cm (cm)	Average area (cm^3)	Deviation from average area C1 (%)	C2 (%)	C3 (%)	C4 (%)	C5 (%)
Volunteer no.							
7	11,0	0,136	63,5	-0,4	-21,0	-20,0	-22,1
9	10,2	0,140	54,0	1,1	-14,2	-16,1	-24,7
59	9,6	0,206	128,0	-0,7	-33,8	-48,3	-45,1
Average	**10,3**	**0,160**	**81,8**	**0,0**	**-23,0**	**-28,1**	**-30,6**
Chiari I patient no.							
43	5,5	0,104	30,0	7,1	-7,5	-14,9	-14,7
5	8,1	0,159	56,0	16,8	-20,0	-34,1	-18,7
26	6,2	0,157	51,3	2,8	-16,4	-18,7	-19,0
11	9,4	0,232	38,6	7,5	-21,6	-18,3	-6,2
21	9,0	0,260	37,6	20,6	-5,0	-25,0	-28,1
58	8,8	0,146	80,2	-7,7	-24,6	-26,1	-21,8
60	9,2	0,176	56,9	-4,7	-19,7	-17,3	-15,3
Average	**8,0**	**0,176**	**50,1**	**6,1**	**-16,4**	**-22,1**	**-17,7**
Postoperative patient							
36	7,7	0,145	72,3	11,8	-26,0	-28,0	-31,0
19	9,8	0,189	66,2	-7,6	-21,4	-22,4	-14,7
18	5,6	0,970	38,7	-16,4	-17,5	-13,1	8,4
Average	**7,7**	**0,435**	**59,1**	**-4,1**	**-21,6**	**-21,2**	**-12,4**

Table 4.2: *Length, average area and tapering in all the studied patients.*

4.1.1 Tapering

Table 4.2 gives the average cross-sectional area for each of the patients, as well as deviation from this average at five different axial levels. Figure 4.3 shows plots of average deviation in each patient-group. We observe that because of the tonsils extensions, on average, the Chiari patients have less variation in cross-sectional flow area than the volunteers. However, when

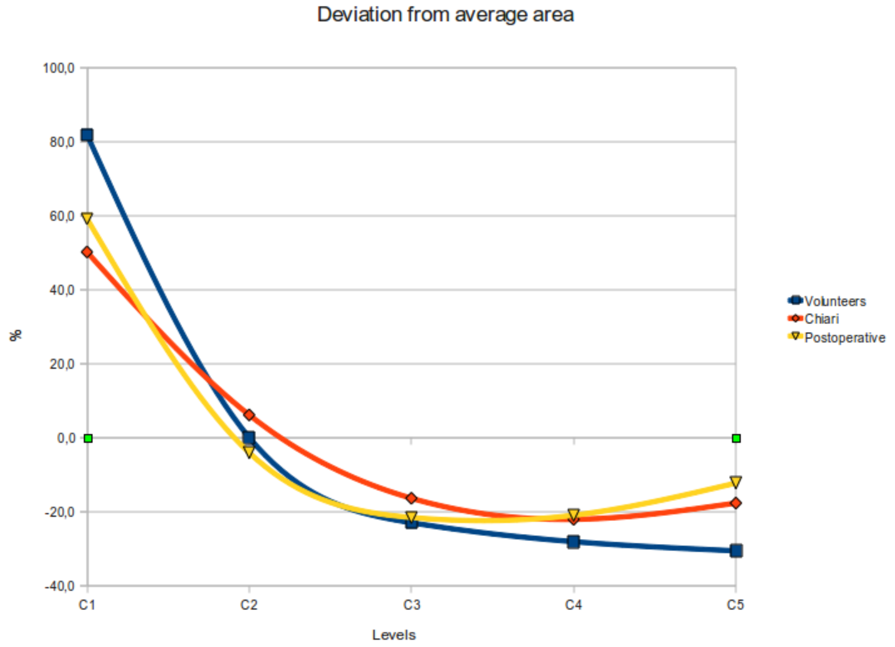

Figure 4.3: *Average tapering in healthy, Chiari I and postoperative groups.*

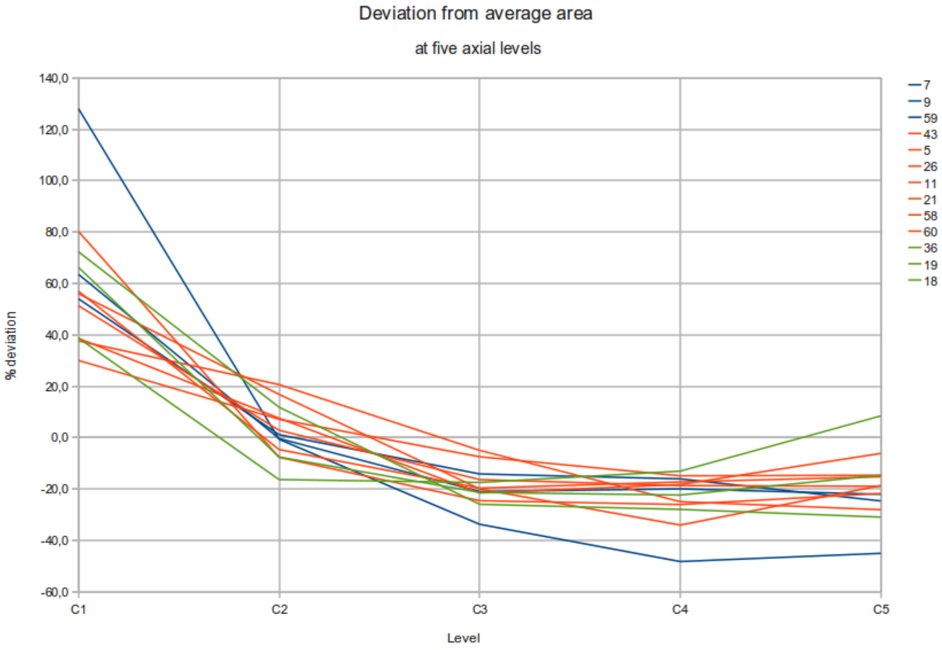

Figure 4.4: *Tapering in all the geometries: Chiari I(red), healthy(blue) and postoperative(green).*

looking at the plot of individual patients (Figure 4.4), we notice that there is one volunteer who has distinctively apparent tapering, while the rest of the volunteers resemble Chiari-patients. A two-tailed t-test conducted at each level, indicates no significant difference in tapering between the three groups ($P > 0.05$).

4.2 Pressure

4.2.1 Pressure during one cardiac cycle

The pressure function is specified at the inflow and the outflow boundaries of the models in such a way that the pressure gradient changes and drives the flow in a pulsatile manner (Figure 4.5). At $t = 0$ s, the pressure difference between the top and the bottom is zero. Then, the pressure increases, with values getting increasingly higher at the top compared to the bottom of the model. This drives the flow downwards (with some time-delay due to inertia), simulating systolic movement of the fluid. At $t = 0.25$ s, the pressure difference is at its peak with ≈ 24.3 Pa higher pressure at the top than at the bottom. Then, the pressure and the pressure difference start decreasing. A reversal occurs at $t = 0.5$, as the pressure at the top of the model starts decreasing faster than at the bottom. This leads to flow-reversal (again after some time-delay), simulating diastolic fluid movement. At $t = 0.75$ s, the pressure difference is again at its maximum, with $\approx$ 24.3 Pa higher pressure at the bottom. After this point in time, the pressure difference decreases again, until $t = 1.0$ s when a new cycle is started.

4.2.2 Pressure distribution inside the models by level

Plotting the average pressure distribution in the three studied groups (Figure 4.6), we observe that on average, the postoperative patients have the most even pressure distribution, with the plot resembling a straight line. For the Chiari patients and the volunteers, the plotted averages appear as more arched curves, with slightly steeper pressure gradients between level 3 and the bottom. Plotting the pressure distributions for all models separately (Figure 4.7), we observe significant variations in pressure distribution in each of the studied groups. A two-tailed t-test conducted between the groups for each axial level indicates significant difference between volunteers and Chiari at levels 2 and 3 ($P \leq 0.01$) with a steeper pressure gradient for Chiari patients. The difference is thus most evident in the upper levels of the anatomy, where the tonsils are. The t-test indicates no significant difference in pressure distribution between Chiari I and postoperative models, nor between healthy and postoperative models.

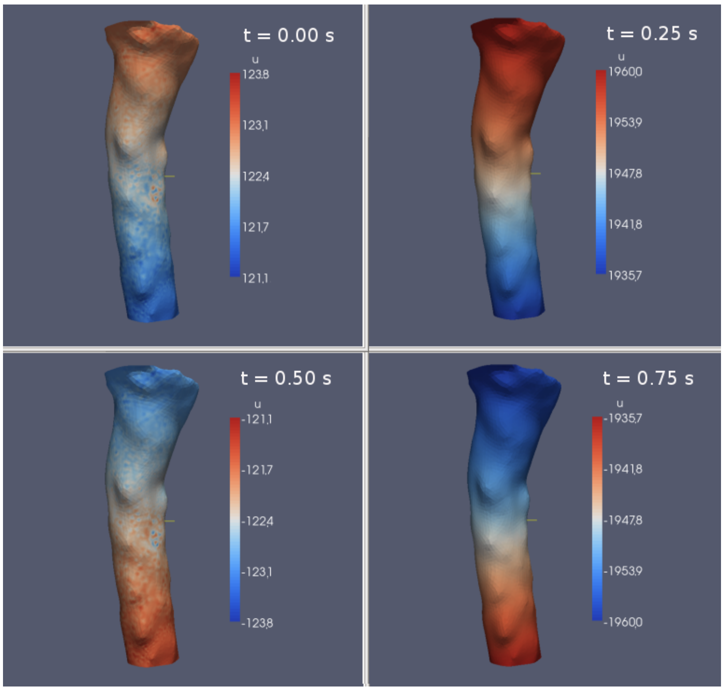

Figure 4.5: *Pressure distribution at four different times during the cardiac cycle.*

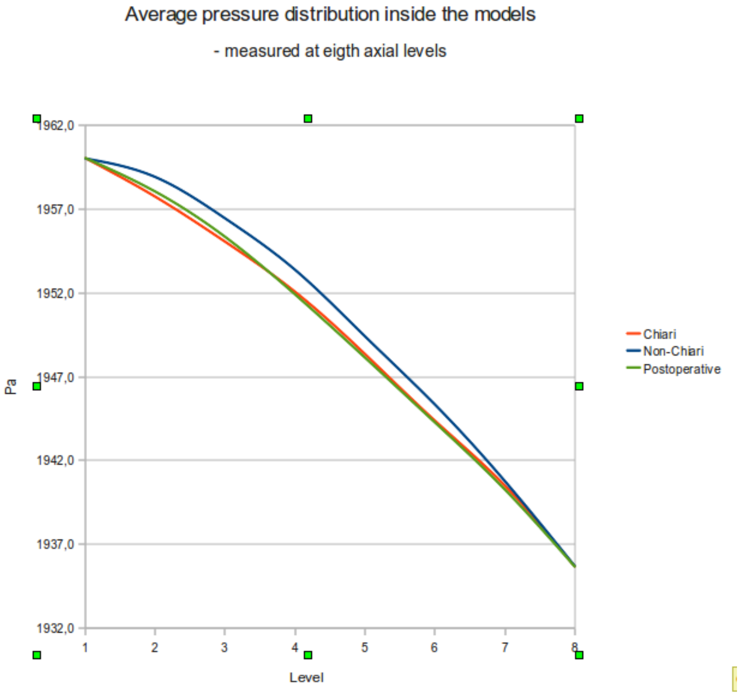

Figure 4.6: *Average pressure distribution by level in the three groups.*

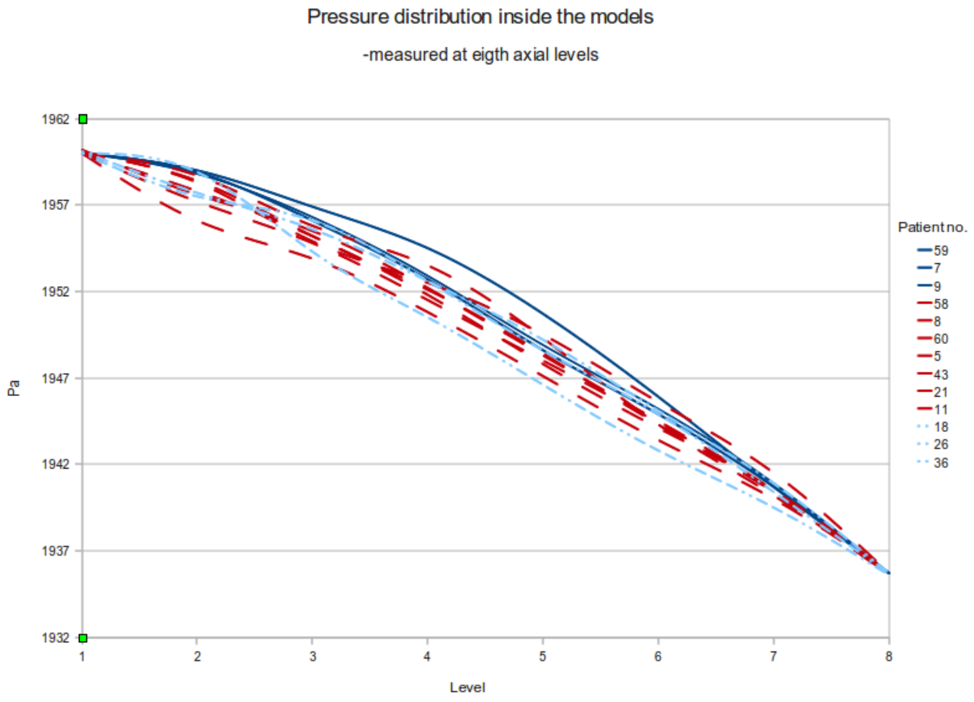

Figure 4.7: *Pressure distribution by level in models of Chiari I patients (red), volunteers (dark blue) and postoperative patients (light blue).*

4.3 Velocities

4.3.1 Velocities during one cardiac cycle

The velocities of the fluid are driven by the changing pressure gradient. However, it takes some time for the velocities to react to the pressure variations. Thus, while the maximum pressure gradient during systole occurs at $t\ = 0.25\ s$, the maximum systolic velocities are observed at $t \approx 0.5\ s$. Equally, while the diastolic pressure-gradient reaches its maximum at $t = 0.75$, the maximum diastolic velocities are observed at $t \approx 1.0\ s$.

We observe differences between systolic and diastolic behavior of the fluid. The systolic velocities have on average slightly higher magnitudes with peak velocities ranging from 6.8 cm/s to 15.6 cm/s. The diastolic velocities range from 6.5 cm/s to 15.7 cm/s. The velocity distributions during diastole differ from velocity distributions during systole (Figure 4.8). Diastolic velocities have the highest magnitudes at the side-boundaries while the systolic velocities appear more visible as they spread more extensively over the axial levels.

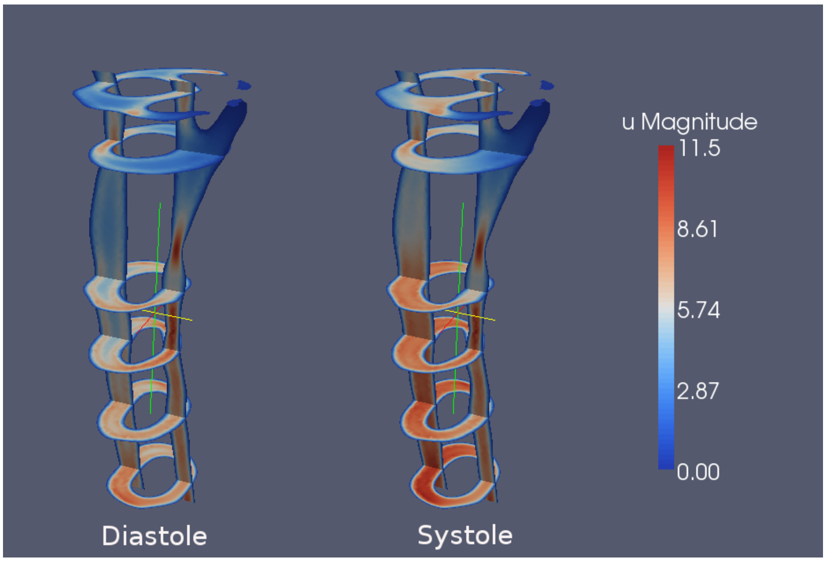

Figure 4.8: *Peak diastolic and systolic velocity magnitudes in a Chiari patient.*

Table 4.9 gives peak systolic and diastolic velocities in all of the studied models.

4.3.2 Peak systolic velocities

In simulations with equal pressure gradients, the systolic peak velocities are on average 27 % higher in Chiari patients than in volunteers. One-tailed t-tests yields a significant difference ($P = 0.002$). Each of the postoperative patients have higher peak systolic velocities than the average peak systolic velocity in volunteers. The postoperative patients have a wide range of velocities ($8.3 - 15.6$ cm/s). One of the postoperative patients has the highest peak velocity of all the thirteen models. A two-tailed t-test yields no significant difference between Chiari-patients and postoperative patients ($P = 0.8$).

Chiari - patients
In models of Chiari patients, peak systolic velocities range from 7.5 cm/s to 12.1 cm/s. Frequently, they appear at several different levels in one geometry. Peak systolic velocities appear at the level of C6, anterior to the cord in five of the seven Chiari models. In four cases, we observe peak velocities at the level of C2-C3, posterior to the cord. In three of the Chiari patients, peak systolic velocities appear also at the level of the foramen magnum, posterior to the cord. High velocity bands are observed at these three locations for most of the Chiari-models.

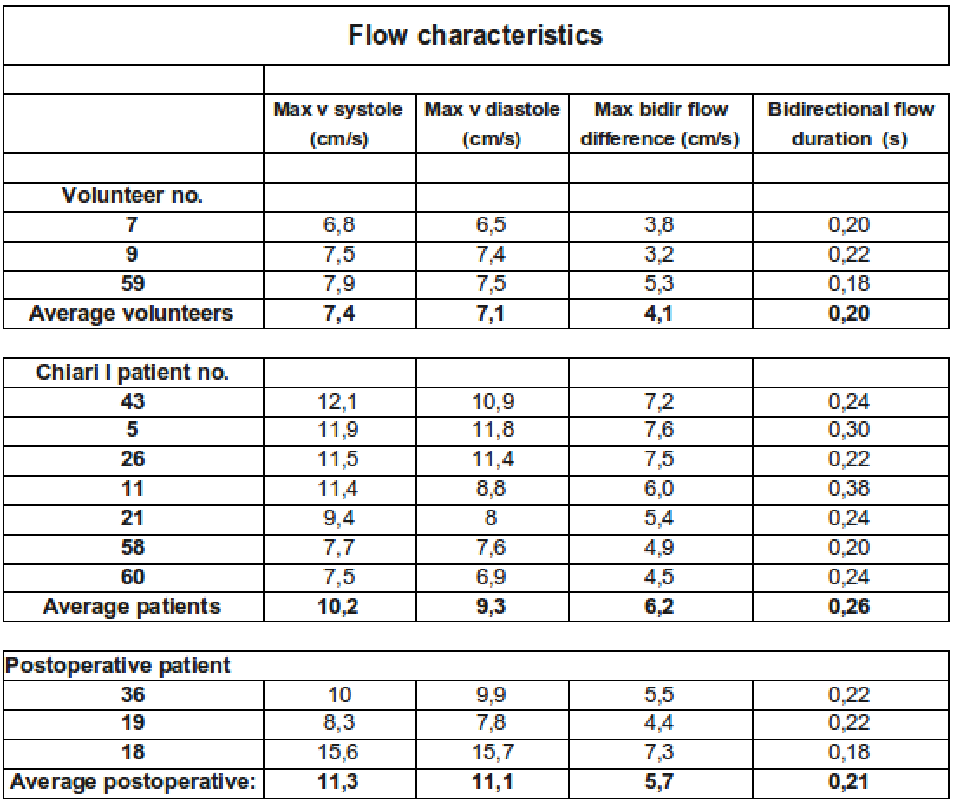

Flow characteristics

	Max v systole (cm/s)	Max v diastole (cm/s)	Max bidir flow difference (cm/s)	Bidirectional flow duration (s)
Volunteer no.				
7	6,8	6,5	3,8	0,20
9	7,5	7,4	3,2	0,22
59	7,9	7,5	5,3	0,18
Average volunteers	**7,4**	**7,1**	**4,1**	**0,20**
Chiari I patient no.				
43	12,1	10,9	7,2	0,24
5	11,9	11,8	7,6	0,30
26	11,5	11,4	7,5	0,22
11	11,4	8,8	6,0	0,38
21	9,4	8	5,4	0,24
58	7,7	7,6	4,9	0,20
60	7,5	6,9	4,5	0,24
Average patients	**10,2**	**9,3**	**6,2**	**0,26**
Postoperative patient				
36	10	9,9	5,5	0,22
19	8,3	7,8	4,4	0,22
18	15,6	15,7	7,3	0,18
Average postoperative:	**11,3**	**11,1**	**5,7**	**0,21**

Table 4.9: *Flow characteristics in all the studied models after simulations with equal pressure gradient for all patients.*

Volunteers

In healthy models, peak systolic velocities range from 6.8 cm/s to 7.9 cm/s. Peak systolic velocities increase gradually from foramen magnum towards the level of C5/6 in all three volunteers. However, in the model with slightly visible tonsils, peak velocities are reached already at the level of C3.

Postoperative patients

In postoperative patients, peak systolic velocities range from 8.3 cm/s to 15.6 cm/s. Their occurrence is very diverse. In one of the models, peak velocities are observed posterior to the cord, at the level of C2 and C3. In the two other postoperative models, peak velocities appear from the level of C2 and down to C5 in bands that switch their position relative to the cord alternately between anterior and posterior.

4.3.3 Peak diastolic velocities

In simulations with equal pressure gradients, peak diastolic velocities are on average 24 % higher in Chiari I patients than in volunteers. One-tailed t-test indicates that this difference is significant ($P = 0.01$). Peak diastolic velocities in all of the postoperative patients are higher than the average peak diastolic velocity in volunteers. Also, two of the postoperative patients have higher peak diastolic velocities than the average peak diastolic velocity in the Chiari I group. The t-test indicates non-significant differences between Chiari and postoperative models ($P = 0.6$). For all the groups, peak diastolic velocities appear towards the model boundaries, contrary to systolic peak velocities that spread along the axial levels.

Chiari patients
Peak diastolic velocities range from $6,9$ cm/s to $11,8$ cm/s in models of Chiari patients. Posterior to the cord, they appear at the same levels as peak systolic velocities. Anterior to the cord, the high velocity bands are less evident than what is observed during systole.

Volunteers
For the volunteers, peak diastolic velocities range from 6.5 cm/s to 7.5 cm/s. They appear at approximately the same levels as peak systolic velocities for all of the volunteers.

Postoperative
The range of peak diastolic velocities is between $7.8 cm/s$ and $15.7 cm/s$ for postoperative patients. Those velocities appear at the same levels as peak systolic velocities.

4.3.4 Velocity patterns

Spatial variations

For all models with visible tonsils, the velocity patterns have common traits when comparing the velocity magnitudes posterior - anterior to the cord (in the sagittal plane). They all characterize by having high velocity bands near the tonsils at the foramen magnum. Then, at the level of C1, the velocities anterior to the cord are higher than posterior to the cord. Further, at the level of C3-C4 the velocity magnitudes are higher posterior to the cord again. Finally, at C5-C6 the velocities anterior to the cord have higher magnitudes.

Figure 4.10 illustrates this pattern in three of the Chiari I models at time of peak systolic flow. Figure 4.11 shows one volunteer and two postoperative patients, all with signs of tonsils at the level of foramen magnum, where the above described pattern occurs.

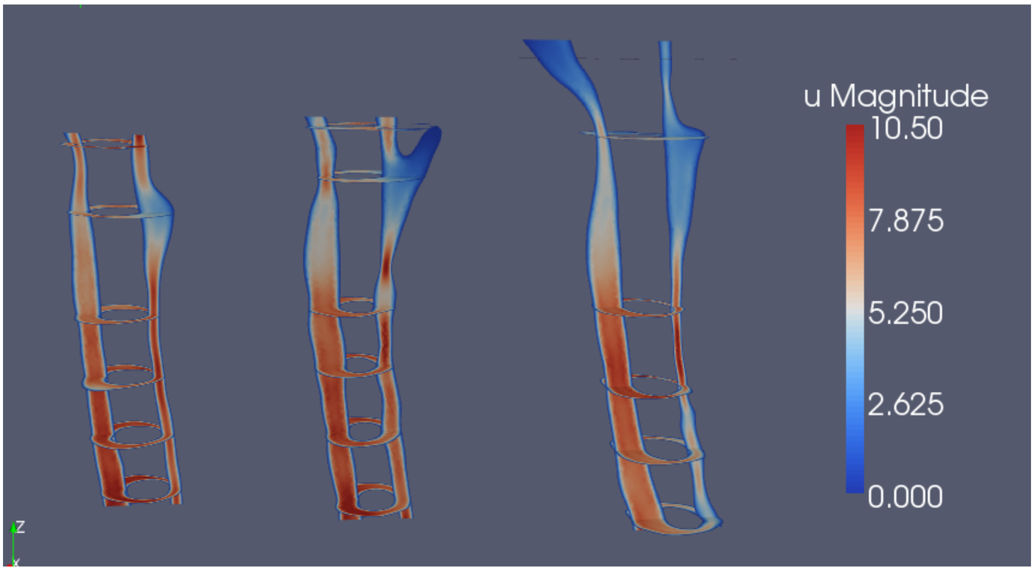

Figure 4.10: *Peak systolic velocity magnitudes in three Chiari patients. The displayed velocity magnitude-range has been rescaled in order to improve visualization.*

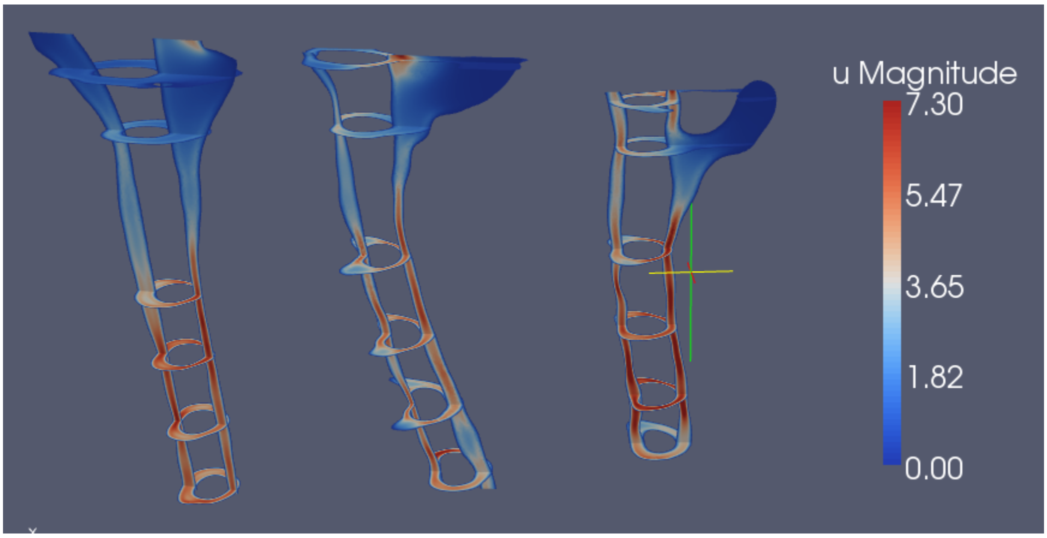

Figure 4.11: *Peak systolic velocity magnitudes in one volunteer (left) and two postoperative patients with signs of tonsils at foramen magnum. The displayed velocity magnitude-range has been rescaled in order to improve visualization.*

For the two healthy models with no visible tonsils (Figure 4.12), the velocity seems to increase progressively from foramen magnum and down to C5/6.

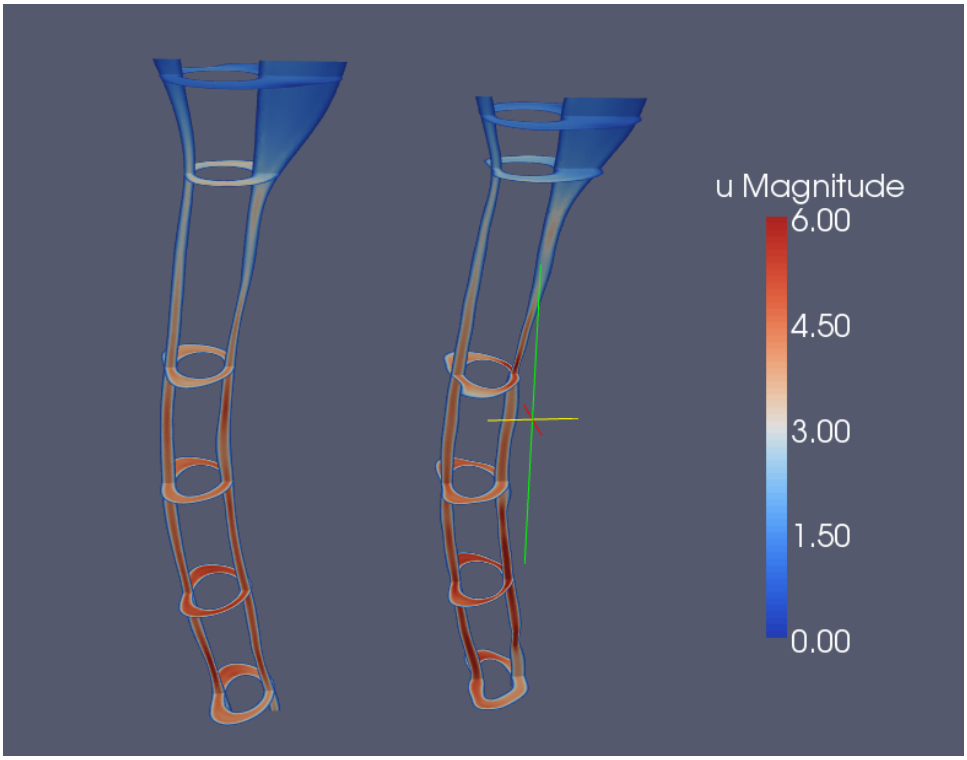

Figure 4.12: *Peak systolic velocity magnitudes in two of the healthy models with no signs of tonsils. The displayed velocity magnitude-range has been rescaled in order to improve visualization.*

Temporal variations

For all three groups, there are evident differences between systolic and diastolic velocity patterns. While systolic velocities spread more along the axial levels, diastolic velocities have higher magnitudes at the side boundaries. However, in Chiari patients, temporal variations are much more evident than in volunteers. Figure 4.13 illustrates peak diastolic and peak systolic velocities in a Chiari-model. We observe e.g. that peak systolic velocities appear at the level of C6, while they don not appear at this level during diastole. Figure 4.14 illustrates peak diastolic and peak systolic velocities in a volunteer. We observe that while the systolic velocities are much more spread along the axial levels, the peak velocities appear at the same level both during systole and diastole.

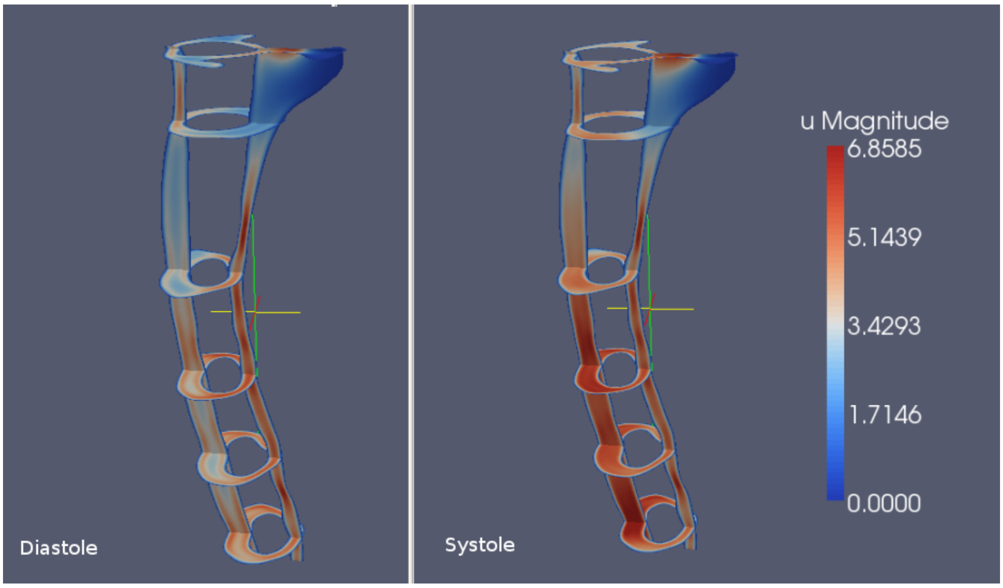

Figure 4.13: *Peak diastolic and peak systolic velocity magnitude patterns in a Chiari model.*

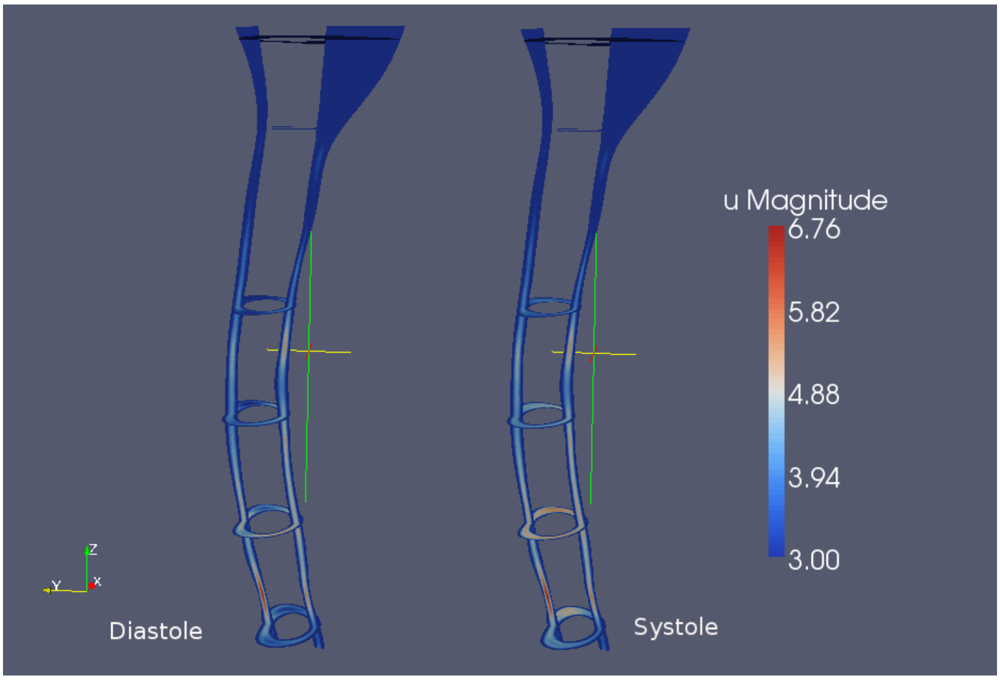

Figure 4.14: *Peak diastolic and peak systolic velocity magnitude patterns in a non-Chiari model.*

Jets

In five of the Chiari patients we observe jets anterolateral to the cord starting from the level of C1/2 down to C6. The jets are not apparent during the whole cardiac cycle but during time of decreasing pressure gradient ($t \in (0.25 - 0.75)\ s$). The size of the jets change with time, as well as their velocity magnitudes in correspondence to the magnitudes in the adjacent area. They are most visible at times of flow reversal and less visible at time of peak systolic flow ($t = 0.5\ s$).

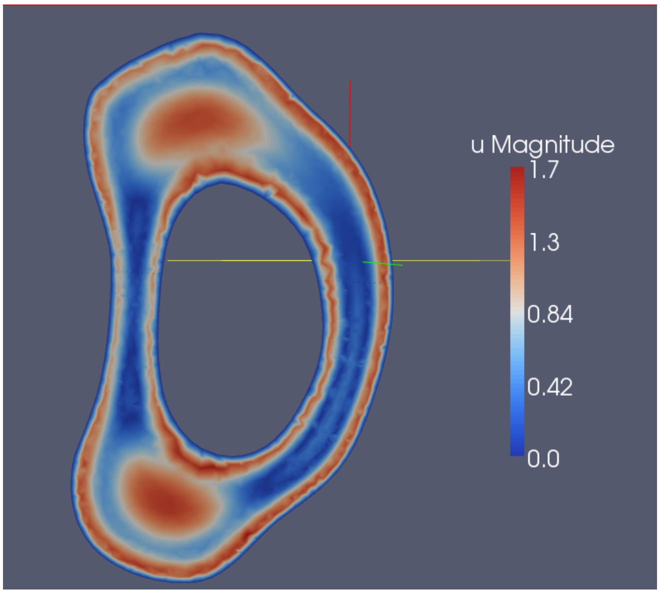

Figure 4.15: *Jets at the level of C3 in a Chiari Patient.*

At time of increasing pressure-gradient, the jets disappear and the velocity magnitudes in the same locations become lower than in the adjacent area.

The jets are found in two of the postoperative models. Figure 4.16 (left) illustrates asymmetric jets at $t \approx 0.60s$ in the cardiac cycle in one of these patients. Figure 4.16 (right) shows the same level at $t \approx 0.20s$, where we observe that the velocity magnitudes change and are now greater in the adjacent area than in the region where the jet occurred.

In two of the volunteers, we find a jet-like pattern anterolateral to the cord (Figure 4.17). However, the jets have a smaller area and more than twice as small velocity magnitudes as the jets in Chiari I models.

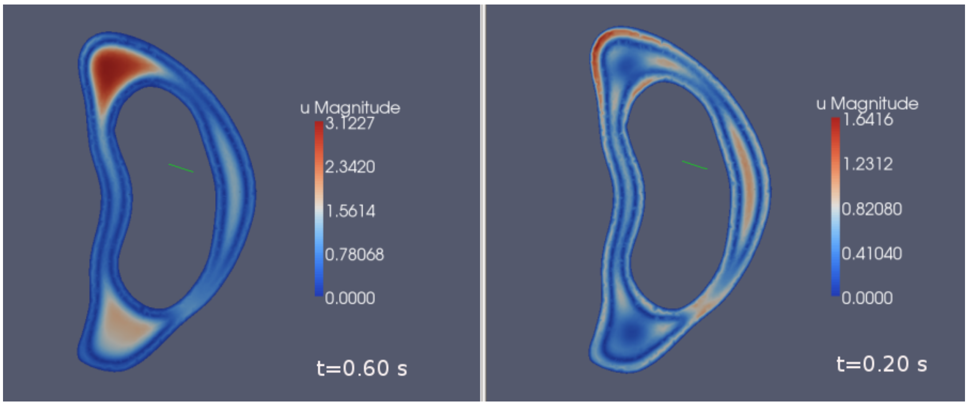

Figure 4.16: *Axial level of C3 in a postoperative patient at different* $t = 0.60$ *s (left) and at* $t = 0.20$ *s (right).*

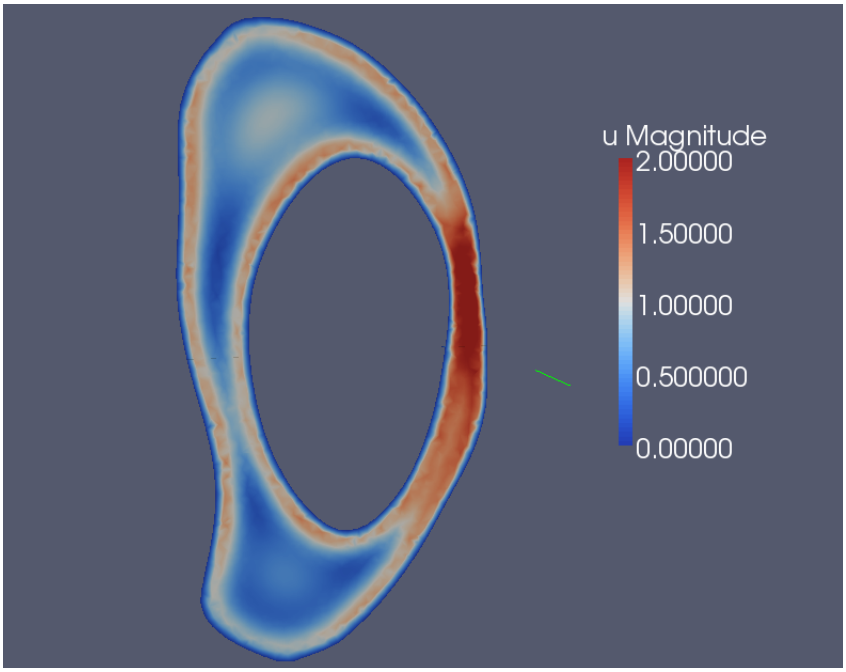

Figure 4.17: *Jet-like pattern anterolateral to the cord at the level of C3 in a volunteer.*

4.4 Synchronous bidirectional flow

Synchronous bidirectional flow occurs at times of flow-reversal and is most visible along the side - boundaries of the channel. Frequently, the magnitude of synchronous bidirectional flow difference reaches its maximum at the levels where maximum systolic or diastolic velocities occur. Figure 4.18 shows synchronous bidirectional flow at the level of C3 in a Chiari-patient during systole at time $t = 0.25$. We observe that the systolic flow (in the negative z-direction) creates two jets anterolateral to the cord.

Synchronous bidirectional flow is found in all the patients and all the volunteers. Table 4.9 gives the maximum difference in velocities and the duration of bidirectional flow for all the studied models after simulations with equal pressure gradients. Maximum difference in synchronous bidirectional flow velocities has on average 34% higher value in Chiari I models than in volunteers; which according to the t-test is a significant difference ($P = 0.03$). The t-test shows no significant differences in synchronous bidirectional flow between postoperative and Chiari-models ($P = 0.7$). Synchronous bidirectional flow at the level of C1 occurs for a longer period of time in six of the Chiari I models compared to the three volunteers. A two-tailed t-test yields P-value equal to the chosen significance-level($P = 0.05$). It is thus questionable if the differences in bidirectional flow durations are significant. The average duration of synchronous bidirectional flow in postoperative patients is $0.01s$ longer than in volunteers and the t-test indicates that this difference is not significant.

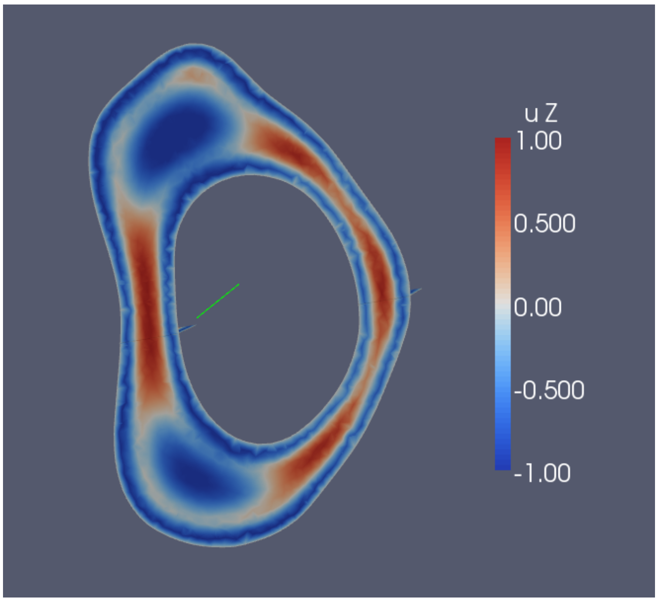

Figure 4.18: *Synchronous bidirectional flow at $t = 0.25$ s at the level of C3 in a Chiari patient.*

4.5 Flux

Maximum flux is found during time of peak systolic velocity. Table 4.19 gives the results of flux computations in all the models after simulations with equal pressure gradients. Average maximum flux for Chiari-patients is 34% larger than in volunteers, and the t-test indicates that this is a significant difference ($P = 0.001$). The postoperative models have on average 19% larger maximum flux than the volunteers and 22% lower flux than the Chiari models. The t-test indicates that the differences in maximum flux are significant between the three groups .

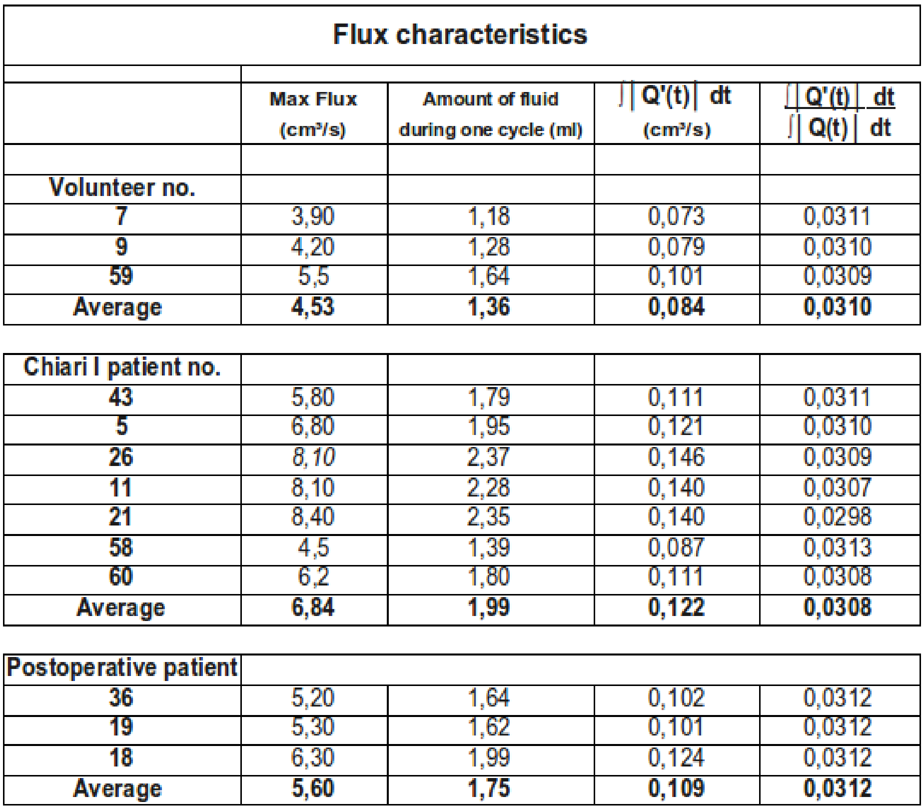

Flux characteristics

	Max Flux (cm^3/s)	Amount of fluid during one cycle (ml)	$\int \lvert Q'(t) \rvert \, dt$ (cm^3/s)	$\frac{\int \lvert Q'(t) \rvert \, dt}{\int \lvert Q(t) \rvert \, dt}$
Volunteer no.				
7	3,90	1,18	0,073	0,0311
9	4,20	1,28	0,079	0,0310
59	5,5	1,64	0,101	0,0309
Average	**4,53**	**1,36**	**0,084**	**0,0310**
Chiari I patient no.				
43	5,80	1,79	0,111	0,0311
5	6,80	1,95	0,121	0,0310
26	*8,10*	2,37	0,146	0,0309
11	8,10	2,28	0,140	0,0307
21	8,40	2,35	0,140	0,0298
58	4,5	1,39	0,087	0,0313
60	6,2	1,80	0,111	0,0308
Average	**6,84**	**1,99**	**0,122**	**0,0308**
Postoperative patient				
36	5,20	1,64	0,102	0,0312
19	5,30	1,62	0,101	0,0312
18	6,30	1,99	0,124	0,0312
Average	**5,60**	**1,75**	**0,109**	**0,0312**

Table 4.19: *Flux-characteristics for simulations with the same pressure gradient for all models.*

The total amount of fluid that flows through the models during one cardiac cycle range between 1.18 *ml* and 2.37 *ml*. The total change in flux is on average larger in Chiari models than in healthy models. However, the ratios between the total change in flow and the total flow volume during one cardiac cycle are similar for all three groups.

4.6 Comparing velocities with MRI measurements

MRI-measurements are available for 7 of the 13 patients. Table 4.20 contains information on how much the velocities computed in simulations with equal pressure gradients differ from the MRI velocity measurements.

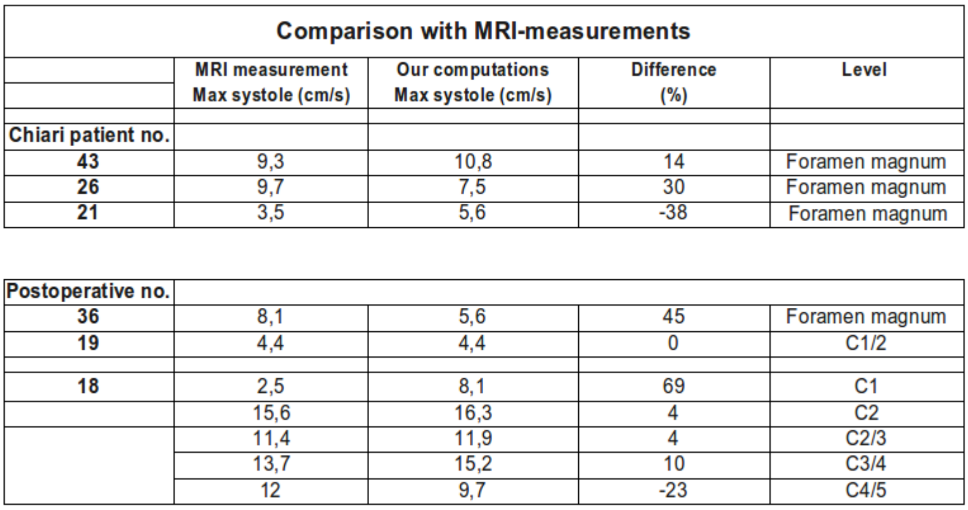

Comparison with MRI-measurements				
	MRI measurement Max systole (cm/s)	Our computations Max systole (cm/s)	Difference (%)	Level
Chiari patient no.				
43	9,3	10,8	14	Foramen magnum
26	9,7	7,5	30	Foramen magnum
21	3,5	5,6	-38	Foramen magnum

Postoperative no.				
36	8,1	5,6	45	Foramen magnum
19	4,4	4,4	0	C1/2
18	2,5	8,1	69	C1
	15,6	16,3	4	C2
	11,4	11,9	4	C2/3
	13,7	15,2	10	C3/4
	12	9,7	-23	C4/5

Table 4.20: *MRI velocity measurements and our computed velocities at time of maximum systolic flow.*

We observe that in models no. 26, no. 21 and no. 36, the differences exceed 30%. For these three patients, we choose to run new simulations with the pressure gradient increased/decreased corresponding to these differences. In postoperative patient no. 18 we observe that the velocity magnitudes in our computations are 69% higher than MRI-measured velocities at the level of C1, while at the level of C4/C5 our computed velocities are 23% lower than the measurements. We choose not to run new simulations for this patient as the velocities at levels C2-C3/C4 do not differ much.

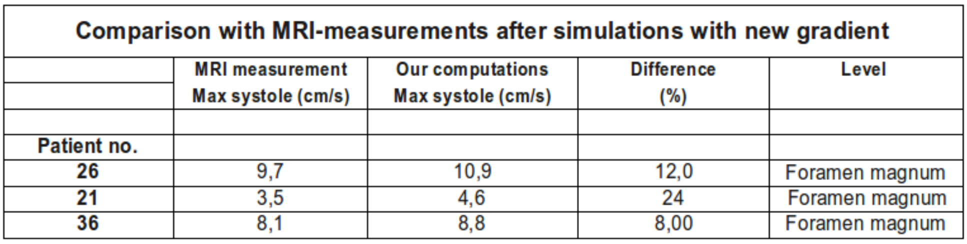

Comparison with MRI-measurements after simulations with new gradient				
	MRI measurement Max systole (cm/s)	Our computations Max systole (cm/s)	Difference (%)	Level
Patient no.				
26	9,7	10,9	12,0	Foramen magnum
21	3,5	4,6	24	Foramen magnum
36	8,1	8,8	8,00	Foramen magnum

Table 4.21:

After the second round of simulations with corrected gradient we observe that in patient 21, the difference between the MRI-measured and the computed velocities is still $> 20\%$ (Table 4.21). This means that the pressure gradient, which already is 38% lower than the originally applied gradient should be further diminished in order to achieve better results. However, it might be questionable if an even smaller pressure gradient is a physiologically realistic choice. Therefore, setting additional conditions on e.g. velocity should be considered in order to achieve more correct results in further simulations on this patient.

Table 4.22 gives flow characteristics after simulations with corrected gradients.

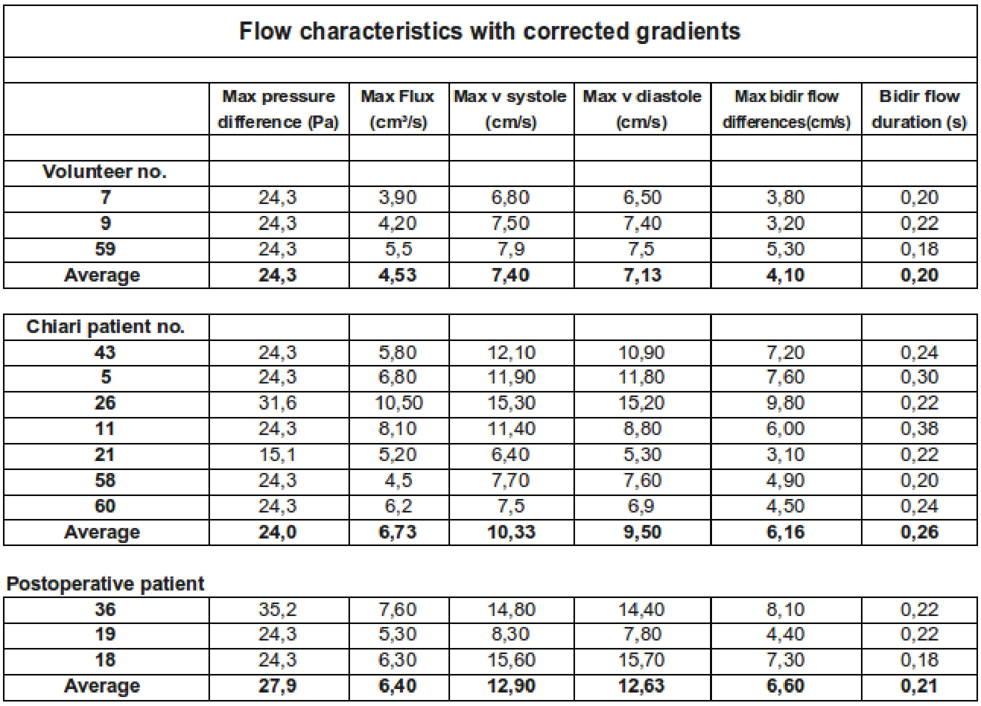

Flow characteristics with corrected gradients

	Max pressure difference (Pa)	Max Flux (cm^3/s)	Max v systole (cm/s)	Max v diastole (cm/s)	Max bidir flow differences(cm/s)	Bidir flow duration (s)
Volunteer no.						
7	24,3	3,90	6,80	6,50	3,80	0,20
9	24,3	4,20	7,50	7,40	3,20	0,22
59	24,3	5,5	7,9	7,5	5,30	0,18
Average	**24,3**	**4,53**	**7,40**	**7,13**	**4,10**	**0,20**
Chiari patient no.						
43	24,3	5,80	12,10	10,90	7,20	0,24
5	24,3	6,80	11,90	11,80	7,60	0,30
26	31,6	10,50	15,30	15,20	9,80	0,22
11	24,3	8,10	11,40	8,80	6,00	0,38
21	15,1	5,20	6,40	5,30	3,10	0,22
58	24,3	4,5	7,70	7,60	4,90	0,20
60	24,3	6,2	7,5	6,9	4,50	0,24
Average	**24,0**	**6,73**	**10,33**	**9,50**	**6,16**	**0,26**
Postoperative patient						
36	35,2	7,60	14,80	14,40	8,10	0,22
19	24,3	5,30	8,30	7,80	4,40	0,22
18	24,3	6,30	15,60	15,70	7,30	0,18
Average	**27,9**	**6,40**	**12,90**	**12,63**	**6,60**	**0,21**

Table 4.22: *Results of simulations with corrected pressure gradients. Values in the first column demonstrate the maximum pressure difference between the top and the bottom of each model resulting from the new pressure gradients.*

The overall results have not changed after the new simulations. The Chiari-patients and volunteers differ in flux, maximum systolic and diastolic velocities and in maximum synchronous bidirectional flow differences. The flow characteristics of Chiari I models have on average higher magnitudes than the characteristics of healthy models in all of the cases. The postoperative models' characteristics do not appear to have significant differences from the

Chiari-models. Further, the differences in duration of bidirectional flow are the same as after previous simulations.

Chapter 5

Discussion

Conclusions

The conducted simulations show differences in flow characteristics of patient-specific Chiari I and normal models. Peak velocities, synchronous bidirectional flow and flux appear to have higher magnitudes in Chiari I models compared to the healthy models. In the upper levels of the anatomy, where the tonsils are, the Chiari I models tend to have a steeper pressure gradient than the volunteers. Postoperative patients' models are similar to those of Chiari patients' in both peak velocities and synchronous bidirectional flow. Differences in the duration of synchronous bidirectional flow are not apparent between the three groups. As no significant differences in tapering have been found, we cannot relate the effect of tapering to our results.

The CSF flow is complex in both Chiari and volunteer models. However, spatial and temporal flow variations are more apparent in Chiari I models. Jets occur in five of the Chiari models and in two of the healthy models, yet are larger, more frequent and have higher magnitudes in the Chiari group. Complex flow patterns and jets occur also in two of the postoperative patients.

Common velocity patterns for models with tonsillar herniations are apparent. Dominance of flow anterior-posterior to the cord appears to depend on the axial level of study. Generally, in tonsil-herniated models, higher velocity bands appear at foramen magnum (posterior to the cord), at C1 (anterior to the cord), at C3/C4 (posterior) and at C5/C6 (anterior). Peak velocities appear in one or several of these locations. For healthy models without sign of tonsils, the velocity patterns are less complex as the velocities increase progressively towards C5/C6.

Concurrence with previous research

Our report on higher peak velocities in Chiari-models compared to those of volunteers agrees with a majority of previous research (e.g. Shah et al. (2011), Hentschel et al. (2010b), Quigley et al. (2004), Haughton et al. (2003)). Further, the more diverse spatial and temporal variations observed in Chiari-models are in accordance with research by e.g. Quigley et al. (2004) who reported that peak systolic and diastolic velocities appear in the same regions in volunteers, while they emerge in distinct regions in Chiari patients. In our Chiari models, the repetitive change in flow domination posterior-anterior to the cord seems not to agree with previous examinations. E.g. Quigley et al. (2004) and Linge et al. (2011) observed higher velocities mainly in the anterior nodes. Observation of jets in the anterolateral locations in five of the Chiari patients corresponds to previous findings by e.g. Roldan et al. (2009), Quigley et al. (2004), Shah et al. (2011). However, the jets in our study have velocity magnitudes that vary during the cardiac cycle and they do not appear visible during the whole cycle.

Synchronous bidirectional flow found mainly along the side-boundaries in both our Chiari models and our normal models is in agreement with findings of Linge et al. (2010). However, we do not find any significant differences in the duration of synchronous bidirectional flow between the three studied groups.

The lack of MRI - data of postoperative patients prior to surgery makes it difficult to make conclusions on outcomes of the surgery. However, we observe that average peak velocities are higher in our postoperative models compared to our Chiari models. Previous studies of postoperative patients have shown that the peak velocities are not always reduced by the surgery. A study on 8 postoperative Chiari I patients conducted by Dolar et al. (2004) has shown overall reduction in peak velocities, however in 3 of the patients either the systolic or the diastolic peak velocity or both increased after surgery.

Limitations of the current study

CFD is a complicated undertaking where many assumptions have to be made and where determining the right complexity of the model is a challenge. Because of limited time, the simulations in this study are conducted for five cardiac cycles and with a time-step of $dt = 0.005$. The method tests conducted (Section 3.8) show that the CSF flow does not stabilize thoroughly during five cycles and that a smaller time-step gives slightly different results.

All simulations are carried out using a symmetric pressure function, which does not give an entirely realistic representation of the cardiac circle. However, testing an asymmetric pressure function on one of the models (Section 3.8) yields fairly equivalent results with respect to peak velocities, synchronous bidirectional flow and flux.

The sample size in this study is rather small, which may limit our statistical power to detect differences. Although we cannot base our conclusions on the t-test, its indications together with our analysis of the results yield fairly visible differences between our Chiari and healthy models. The patients studied are not a homogeneous group with respect to age or gender. Those factors may have an impact on the CSF velocities (e.g. Shah et al. (2011)) and would need further analysis.

The boundaries in our models are rigid, while the cord and tonsils are known to move and deform with the pulsating CSF. For a more realistic result, this could be changed in further research. However, it has been suggested that the boundaries' movement is relatively small compared to the dimensions of the cord (Levy, 1999).

Significance

The method presented in this study yields a noninvasive approach for verifiable measurement of the CSF velocities in real patients. Combined with (and adjusted according to) MRI-measurements it gives the advantage of studying the results globally or locally at a desired point in time in any chosen plane. During result-analysis, we notice that in measurements of peak velocities, velocity magnitudes may change significantly between locations that are within small distance from each other. Thus, using solely the MRI-measurements might give unrealistic impression of the CSF velocities in patients. E.g. in our model of patient no. 26, the computed peak systolic velocity was 37% higher than the single level MRI peak velocity measurement. Further, two different models may have equal patterns and velocities at one level and differ significantly at another level. It is thus a great advantage to be able to study a whole volume instead of just one cross-section of a model.

The good temporal and spatial resolutions allow a more detailed examination of synchronous bidirectional flow and of variations in velocity patterns compared to MRI-measurements. We observe that the magnitude of synchronous bidirectional flow changes along the anatomy, thus an MRI-measurement at a single axial level might not give a realistic impression of the amount of bidirectional flow in a patient.

This study adds additional validation to CFD studies of CSF flow which indicate greater CSF velocities and different flow characteristics for Chiari patients than for healthy individuals. It also demonstrates significant individual differences, even in patients belonging to the same groups.

Further research

Additional simulations of CSF flow supplemented by MRI-measurements can lead to improved ability to distinguish pathologic flow abnormalities that cause syringomyelia, and the diverse symptoms in Chiari I malformation. Generation of patient-specific models both prior- and post-surgery could give a better understanding of outcomes of cranio-vertebral decompression and possibly a better categorization of Chiari-related conditions that demand surgery. In addition, it might be of interest to compare patients and volunteers of the same gender and age in order to remove the influence of these possibly significant factors.

According to Oldfield et al. (1994), syrinxes start at about 5 cm below the foramen magnum. As none of our Chiari I models have syrinxes inside their spinal canals, we cannot evaluate the possible effects of syringomyelia on velocity and pressure distributions. The method test with applied uneven pressure gradient (Section 3.8) implies that setting a 20% higher pressure gradient posterior to the cord at the level of foramen magnum, does not seem to affect the CSF velocities in the other axial levels in a major way. Conducting further tests of this kind, with higher gradient differences could perhaps yield a better understanding on the piston effect of the tonsils on the CSF velocities.

As seen from comparison with MRI velocity measurements, setting boundary conditions based solely on pressure does not always yield realistic results. For further studies, it is there for recommended to set initial and boundary conditions on both pressure and velocity based on MRI measurements.

Bibliography

W. S. Ball and K. R. Crone. Chiari I malformation: From Dr Chiari to MR Imaging. *Radiology*, 195:602–604, 1995.

B. Battal, M. Kocaoglu, N. Bulakbasi, G. Husmen, H. Tuba Sanal, and C. Tayfun. Cerebrospinal fluid flow imaging by using phase-contrast MR technique. Br J Radiol [Epub ahead of print], May 2011.

G. K. Bejjani. Definition of the adult Chiari malformation: a brief historical overview. *Neurosurgery rev*, 11(1):251–264, 2001.

J. Cousins and V. Haughton. Motion of the cerebellar tonsils in the foramen magnum during the cardiac cycle. *AJNR Am J Neuroradiol*, 30(8):1587–8, 2009.

M. T. Dolar, V. Haughton, B. Iskandar, and M. Quigley. Effect of craniocervical decompression on peak CSF velocities in symptomatic patients with Chiari I malformation. *AJNR Am J Neuroradiol*, 25:142–145, January 2004.

D. Greitz. Unraveling the riddle of syringomyelia. *Neurosurgery rev*, 29: 251–264, 2006.

M. Griebel, T. Dornseifer, and T. Neunhoeffer. *Numerical Simulations in Fluid Dynamics - A practical introduction.* SIAM, 1998.

P. Hall, M. Turner, S. Aichinger, P. Bendick, and R. Campbell. Experimental syringomyelia: the relation between intraventricular and intrasyrinx pressures. *J Neurosurg*, 52:812–7, 1980.

V. Haughton, F.R. Korosec, J.E Medow, M. T. Dolar, and B. Iskandar and. Peak systolic and diastolic CSF velocity in the foramen magnum in adult patients with Chiari I malformations and in normal control Participants. *AJNR Am J Neuroradiol*, 24(2):169–76, Feb 2003.

C. Hayhurst, O. Richards, H. Zaki, G. Findlay, and T. J. Pigott. Hindbrain decompression for Chiari - Syringomyelia complex: an outcome analysis comparing surgical techniques. *Br J Neurosurg*, 22(1):86–91, Feb 2008.

J. D. Heiss, N. Patrons, H. L. Decroom, T. Shaker, R. Ennis, W. Hammerer, A. Eidetic, T. Talbot, J. Morris, E. Eskimo, and E. H. Oldfield. Elucidating the pathophysiology of syringomyelia. *J Neurosurgery*, 91(4):553–62, October 1999.

S. Hentschel, S. Linge, A. E. Løvgren, and K. A. Mardal. Cerebrospinal Fluid Flow. from Automated Scientifc Computing (Logg, Mardal, Wells et al.), preliminary draft, September 1., 2010a.

S. Hentschel, K. A. Mardal, A. E. Løvgren, S. Linge, and V. Haughton. Characterization of cyclic CSF flow in the foramen magnum and upper cervical spinal canal with MR flow imaging and computational fluid dynamics. *AJNR Am J Neuroradiol*, 31(6):997–1002, 2010b.

R. Labuda. *Conqueer Chiari: A Patient's Guide to the Chiari Malformation*. C&S Patient Education Foundation, 2008.

D. Levine. The pathogenesis of syringomyelia associated with lesions at the foramen magnum: a critical review of existing theories and proposal of a new hypothesis. *J Neurol Sci.*, 220(1-2):3–21, 2004.

L. M. Levy. MR Imaging of cerebrospinal fluid flow and spinal cord motion in neurologic disorders of the spine. *The Lumbar Spine*, 7:573–587, 1999.

L. M. Levy. Toward an understanding of syringomyelia: MR imaging of CSF flow and neuraxis motion. *AJNR Am J Neuroradiol*, 21(1):45–6, 2000.

S. Linge, V. Haughton, A. E. Løvgren, K. A. Mardal, and H. P. Langtangen. CSF flow dynamics at the craniovertebral junction studied with an idealized model of the subarachnoid space and computational flow analysis. *AJNR Am J Neuroradiol*, 31:185–92, 2010.

S. Linge, V. Haughton, K. A. Mardal, A. Helgeland, and H. P. Langtangen. Effect of tonsilar herniation on cyclic CSF flow studied with computational flow analysis. Accepted for publication in American Journal of Neuroradiology, 2011.

A. Logg, K. A. Mardal, and Wells. Automatic Scientific Computing. Preliminary draft, September 1, 2010.

N. Di Lorenzo, L. Palma, E. Paletinsky, and A. Fortuna. "conservative" cranio-cervical decompression in the treatment of Syringomyelia-Chiari I complex: A prospective study of 20 adult cases. *Spine*, 20(23), December 1995.

T.H. Milhorat and P. A. Bolognese. Tailored operative technique for Chiari type I malformation using intraoperative color Doppler ultrasonography. *Neurosurgery*, 53(4):899–905, discussion 905–6, October 2003.

T. Morvan. *Simula Vmtk Extensions Users Guide*, 2009.

D.M. Mueller and J.J. Oró. Prospective analysis of presenting symptoms among 265 patients with radiographic evidence of Chiari malformation type I with or without syringomyelia. *J Am Acad Nurse Pract*, 16(3): 134–8, March 2004.

E. H. Oldfield, K. Murasaki, and T. H. Shaker and. Psychophysiology of syringomyelia associated with Chiari I malformation of the cerebellar tonsils: implications for diagnosis and treatment. *J Neurosurgery*, pages 803–15, 1994.

M. F Quigley, B. Iskandar, M. A. Quigley, M. Nicosia, and V. Haughton. Cerebrospinal fluid flow in foramen magnum: Temporal and spatial patterns at MR imaging in volunteers and in patients with Chiari I malformation. *Radiology*, 232:229–236, 2004.

A. Roldan, O. Wieber, V. Haughton, T. Osswald, and N. Chesler. Characterization of CSF hydrodynamics in the presence and absence of tonsillar ectoplasm by means of computational flow analysis. *AJNR Am J Neuroradiol*, 30:941–46, 2009.

S. Shah, V. Haughton, and A. Munoz del Rio. CSF flow through the upper cervical spinal canal in Chiari I malformation. *AJNR Am J Neuroradiol*, April 2011.

J.D. Stephany, J.C. Garavaglia, and G. S. Pearl and. Sudden death in a 27-year-old man with Chiari I malformation. *Am J Forensic Med Pathol*, 29(3):249–50, September 2008.

K. Valen-Sendstad, K. A. Mardal, H. Barayanan, and M. Mortensen. A comparison of some common finite element schemes for the incompressible Navier Stokes equations. Automated Scientific Computing (Logg, Mardal, Wells et al), preliminary draft, September 1, 2010.

J. Xie, C. Ma, H. Shan, M. Song, B. Liu, and X. Chen. Craniovertebral decompression and posterior fossa reconstruction treatment of Chiari syringomyelia complex. *Zhonghua Wai Ke Za Zhi*, 38(5):363–5, May 2000.

http://www.vmtk.org/

http://rsb.info.nih.gov/ij/

http://www.openoffice.org/

http://www.paraview.org/

http://www.fenicsproject.com/

https://launchpad.net/nsbench/